Radial Analyte Concentration in Microfluidics with an Integrated Planar Nanoporous Film

by

Brent Scarff
BSc, University of Calgary, 2005

A Thesis Submitted in Partial Fulfillment
of the Requirements for the Degree of

MASTER OF APPLIED SCIENCE

in the Department of Mechanical Engineering

Supervisory Committee

Radial Analyte Concentration in Microfluidics
with an Integrated Planar Nanoporous Film

by

Brent Scarff
BSc, University of Calgary, 2005

Supervisory Committee

Dr. David Sinton (Department of Mechanical Engineering)
Supervisor

Dr. Sadik Dost (Depertment of Mechanical Engineering)
Departmental Member

Dr. Tao Lu (Department of Electrical and Computer Engineering)
Outside Member

Abstract

Supervisory Committee

Dr. David Sinton (Department of Mechanical Engineering)
Supervisor

Dr. Sadik Dost (Depertment of Mechanical Engineering)
Departmental Member

Dr. Tao Lu (Department of Electrical and Computer Engineering)
Outside Member

This work revolves around the development of microfluidic technology for use in biomedical diagnostics with a specific focus on analyte concentration. At the reduced scale inherent with microfluidic technologies the sensing of target species can be difficult since the sample volume is reduced to nanolitres leading to low amounts of target species. This necessitates the need to preconcentrate samples prior to the sensing step. The exclusion-enrichment phenomenon associated with concentration polarization has been used within microfluidic platforms for the purpose of analyte concentration though methods have all been inherently 1-D, axial configurations.

Within this work a novel radial concentration strategy based on a single microfluidic layer on a uniform nanoporous film is presented. The active nanostructured region is defined by the microfluidics, providing flexibility and opening opportunities beyond the single-channel axial configurations to date. Radial geometries have not been previously shown operating as CP based concentration devices, though the unique geometry offers enhanced flux at the perimeter and the capability to focus samples down to small central regions. This focusing ability allows the concentration to take place on a

separate layer and does not compete for space with other analysis fluidics. This radial configuration is numerically modeled and experimentally demonstrated.

Table of Contents

List of Tables

List of Figures

Nomenclature

c_i	concentration of species i
c_i^0	bulk concentration of species i
e	charge of an electron, $1.6022 \times 10^{-19}\ C$
h_{ch}	channel height
h_m	membrane height
k	Boltzmann's constant, $1.3807 \times 10^{-23}\ J\ K^{-1}$
u	velocity
r	radial coordinate
r_p	pore radial coordinate
t	time
t_{acc}	accumulation time
z_i	valence number of species i
A_p	pore cross sectional area
C_0	bulk concentration
C^*	normalized concentration
D	diffusion coefficient
$\vec{E}$	electric field vector
F	Faraday's constant, $96485\ C\ mol^{-1}$
J	flux
L	characteristic length
P	pressure

Q_{ch}	channel flow rate
Q_m	membrane flow rate
R	universal gas constant, $8.314\ J\ K^{-1}\ mol^{-1}$
R	channel radius
R_p	pore radius
R_{acc}	accumulation rate
T	temperature
U_{EO}	electroosmotic velocity
U_{EPH}	electrophoretic velocity
α	degree of dissociation
ϵ_0	permittivity of vacuum, $8.8542 \times 10^{-12}\ C\ V^{-1}\ m^{-1}$
ϵ_r	relative permittivity
ϵ_w	porosity
ϕ	electric potential due to an applied electric field
γ	interfacial tension
κ	conductivity
λ	Debye length
μ	viscosity
ν_{eff}	effective mobility
ν_i	mobility of ionic species i
ρ	density
ρ_e	charge density
σ	surface charge density

σ_{ch}	channel surface charge density
σ_m	membrane surface charge density
ψ	electrical potential due to the presence of the electric double layer
ζ	zeta potential
$\langle ... \rangle$	area averaged quantity

Acknowledgments

I would like to express my deep gratitude to several people who helped make this work possible. First I thank my supervisor, Dr. David Sinton, for his guidance, enthusiasm and encouragement. I would also be at a loss if it were not for the members of the microfluidics lab group, past and present, who paved the way and lent me there insights into the nuances of fabrication and experimentation. Finally, I must thank my family for instilling in me the work ethic required successfully complete this work and my friends for their endless patience and continued support.

Chapter 1. Introduction

1.1 Background and Motivation

With the fabrication of microchannels (channels with dimensions of tens to hundreds of micrometers) in the early 1990's [1] the realm of microfluidics has matured into a field and garnered the attention of chemists, biologists and engineers [2]. Interest and applications have grown, particularly in the areas of biotechnology and chemical analysis where large numbers of experiments can be carried out with small quantities of reagents in less time [3]. Microfluidics is thought to have the potential to significantly change the way modern biology is performed [4] and when used as a diagnostic device it has the ability to improve public health [5]. It is this last point regarding public health that has gained recent attention by several groups and papers [5-8]. Microfluidic devices are particularly well suited to these diagnostic applications due to the complex fluid manipulations involved and their inherent portability. With the potential to achieve high levels of integration on a single device diagnostics could be performed with little human intervention giving rise to the so called lab-on-chip concept [9]. This drive towards portability at low cost has implications not only for first world health and military but also the developing world.

Just as with the micro-electronics movement the goal now is to achieve ever more complex functions at highly reduced scales. However, as fluid channel sizes are scaled down to the microscale, the governing physics differ significantly from macroscale fluid mechanics, particularly due to the dominance of surface forces over volume forces at small scales [10]. With this in mind some of the fundamental physics on the microscale

should be understood to properly leverage the various phenomena observed and create ever more innovative and efficient microfluidic components.

This work revolves around the development of microfluidic technology for use in biomedical diagnostics with a specific focus on analyte preconcentration. The primary aim is the demonstration of a novel multidimensional concentration strategy utilizing a planar nanoporous film and radial microfluidic channel structure. A 1D continuum based model is used to guide and optimize the experimental efforts.

1.2 Microfluidic Transport

This section provides a general overview of the transport phenomena relevant to the core contributions in this work (chapters 2-4). Specific attention is paid to those areas that differentiate microfluidics from classical fluid dynamics. Chapter 2 provides a more in depth analysis of microfluidic transport theory and its application.

1.2.1 The Scaling Effect

"The effect of gravity and inertia dominate our experience of the physical world."[8]

The physics that dominate scaled down micro systems are quite different than those macro scale systems we are capable of observing on a day to day basis [10, 11]. To get an indication of what potential benefits can be derived from a reduction in scale one needs only look to nature. Evolution has evolved organisms to maximize internal efficiencies by reducing transport distances and increasing surface areas across which information can be exchanged with the outside environment, effects derived from a simple reduction in scale [12]. A natural question to ask then is why does a change in scale result in such favourable outcomes in terms of efficiencies? To get an indication of

this in terms of fluid flows it is useful to introduce some key dimensionless values that start to shed light on how scale can influence the relative importance of certain physical phenomena. Namely, the dimensionless parameters of relevance are the Reynolds number, the Capillary number and the Peclet number.

1.2.2 Reynolds Number and Laminar Flows

The Reynolds number is defined as:

$$\mathrm{Re} = \frac{\rho u L}{\mu} \tag{1.1}$$

where ρ is the density, u is the characteristic velocity, μ is the viscosity and L is the characteristic length. The Reynolds number is a ratio of inertial to viscous forces in a flowing fluid hence the magnitude of this number gives an indication as to the dominant forces at work. Characteristic lengths and velocities in microchannel flows are such that the Reynolds numbers are small (often $\ll 1$) indicating flow is strongly laminar and viscous forces dominate. A major result of this type of flow regime is illustrated in how multiphase flows interact, namely the convective forces responsible for mixing in inertial flows are negligible [4, 11]. In laminar flow two streams interact across their interface purely by the Brownian motion of their particles resulting in a diffusive process that equalizes the concentrations over spatial gradients with time. This diffusion process can be characterized in one dimension as:

$$d^2 = 2Dt \tag{1.2}$$

where D is the diffusion coefficient and d is the distance a particle moves in time t. The key element to take from equation (1.2) is that time increases with the square of distance. Large scale phenomena are largely unaffected by diffusion processes simply because the

time for molecules to travel meaningful distances is extremely long. However, scaling the dimensions down to micrometers corresponds to a drastic reduction in process time. As an illustration of this effect, a small molecule in aqueous solution is expected to diffuse a net displacement of 10 mm in 15 minutes, diffusion on the scale of $10\,\mu m$ however occurs on the order of 100 ms [13].

In microfluidic flows the laminar flow and associated diffusion phenomena are beneficial in some applications but in other instances they may prove to be obstacles. For instance many applications require that streams be mixed at rates faster than diffusion alone can afford. When mixing streams is the goal the processes of interest are those of diffusion and convection. The Peclet number is another convenient dimensionless parameter that quantifies these relative effects and can be defined in the following manner:

$$Pe = \frac{uL}{D} \tag{1.3}$$

where variables are as defined previously. To create effective mixing schemes the goal is often to increase the convective term by increasing fluid velocity and/or manipulating geometry. Passive and active mixers have been devised and are often a key component in microfluidic systems [14, 15]. Passive methods often use clever geometric configurations to intertwine and fold streams where as active methods can use electrokinetic effects, pressure driven effects or electro-wetting effects to name a few [14, 16].

1.2.3 Surface Forces

The next key component to understanding physics on microscales lies in interfaces [17, 18]. All substances have an interface across which they interact with the rest of the

world. On the macro scale the role of the interface is often small compared with the volume-based forces that act on the bulk of the material (such as gravity). However, as device dimensions get smaller the surface area to volume (SAV) ratio grows. Considering again a reduction in length scale from $1\ mm$ down to $10\ \mu m$ results in an increase in SAV ratio of $10\ 000\times$ [13]. The large change in the SAV ratio corresponds to a significant increase in the effect of surface forces at the microscale making interfaces extremely important. A dimensionless parameter that characterizes these effects is the capillary number. This relates viscous forces to interfacial forces across immiscible boundaries and is defined as:

$$\mathrm{Ca} = \frac{\mu u}{\gamma} \tag{1.4}$$

where γ is the interfacial tension. High capillary numbers indicate viscous forces are dominant and low numbers indicate interfacial forces dominate [19]. A somewhat counter-intuitive demonstration of the dominance of surface forces at small scales was performed in the early 90's by showing that water can travel autonomously uphill simply by manipulation of the interfacial forces [20].

A drawback to the high SAV ratio is in applications where molecules adsorb to channel surfaces since the area which is available for exchange is much higher and thus adsorption rates can be significant. Specifically in pressure driven flows this adsorption can be severe and surface treatments may be required or alternative approaches may need to be looked at [21]. One such alternative is the use of electrokinetic transport since it provides higher shear forces at surfaces, limiting non-specific adsorption [22].

1.2.4 Pressure Driven Flow

Pressure driven flow has of course been well characterized in classical fluid mechanics and many aspects of the flow character remain the same at the microfluidic scale. The Navier-Stokes equations provide a convenient tool to characterize the flow and for steady incompressible, Newtonian fluids with constant properties in time these equations can be written as

$$\vec{\nabla} \cdot \vec{u} = 0 \tag{1.5}$$

$$\rho(\vec{u} \cdot \vec{\nabla})\vec{u} = -\nabla P + \mu\vec{\nabla}^2\vec{u} + F_b \tag{1.6}$$

where $\vec{u}$ is the fluid velocity, P is the pressure and μ, ρ and F_b are the viscosity, density and body force respectively. For laminar flows the convective terms (left side of equation (1.6)) can be neglected due to the dominance of viscous forces at low Reynolds numbers. This simplification reduces the equation to the familiar Stokes flow or Poiseuille flow for straight circular channels [11]. For the case of Poiseuille flow of a Newtonian fluid of constant viscosity equation (1.6) reduces to

$$\frac{dP}{dz} = \mu\left(\frac{d^2u}{dr^2} + \frac{1}{r}\frac{du}{dr}\right) \tag{1.7}$$

For internal pipe flow pressure varies only in the axial direction and with no slip boundary conditions the velocity profiles for these types of flows are parabolic with an analytical solution

$$u(r) = -\frac{1}{4\mu}\frac{dP}{dz}(R^2 - r^2) \tag{1.8}$$

where z is the axial coordinate, r is the radial coordinate and R is the channel radius. In terms of microfluidic applications this flow profile can be undesirable as it leads to dispersion effects which can adversely affect separation applications [3, 23, 24].

1.2.5 The Electric Double Layer

When a fluid comes into contact with a solid interface the dissociation of surface groups and the specific (nonelectric) adsorption of ions to the surface causes a net surface charge [24-26]. This net charge will in turn influence the distribution of ions in the vicinity whereby counterions will be repelled and coions will be attracted. The formation of this screening layer is characterized by the magnitude of the surface charge balanced with the thermal agitation of the system and is commonly known as the electric double layer (EDL). The thickness of the EDL layer is characterized by the Debye length

$$\lambda = \sqrt{\frac{\epsilon_0 \epsilon_r \mathrm{RT}}{2z^2 \mathrm{F}^2 \mathrm{C}_0}} \tag{1.9}$$

Where $\epsilon_0$and ϵ_r are the permittivity of vacuum and the relative permittivity of the medium, R is the universal gas constant, T is the temperature, F is Faraday's constant, z is the ion valence and C_0 is the concentration of the bulk fluid. For moderately dilute solution at 25^0C this term is typically of the order 1-10 nm. Most common descriptions of the EDL account for 2 layers, an inner immobile layer of adsorbed ions known as the Stern layer and a diffuse mobile layer known as the diffuse or Gouy-Chapman layer [24, 27]. The plane separating the mobile ions from the immobile ions is known as the shear plane, the potential at this plane is characterized by the zeta potential (ζ). Figure 1-1 illustrates the various components of the EDL.

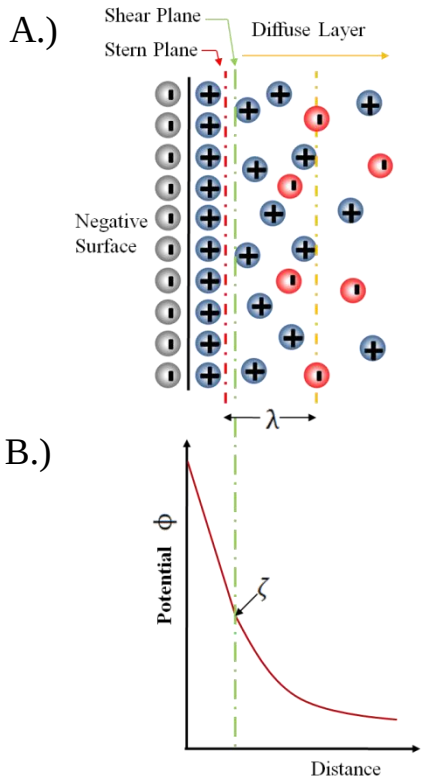

Figure 1-1| (**A**) The structure of the EDL with inner Stern layer and the outer Diffuse layer. (**B**) The electrostatic potential distribution within the EDL, the zeta potential is indicated at the shear plane.

1.2.6 Electroosmotic Flow

Microfluidics makes use of the reduction in scale to manipulate fluids and particles exploiting the interaction of the EDL and applied electric fields. Application of an electric field across a channel will not exert a force on the bulk fluid but the charged fluid in the EDL is acted upon inducing a shear at the edge of the thin Stern layer. The bulk of the fluid is in turn induced to flow through viscous interaction with the flowing fluid in the EDL. A steep velocity gradient is generated in the vicinity of the wall as a result of the no slip interaction with the solid surface generating high shear stresses at the shear plane. This results in a velocity profile that is plug-like and less susceptible to dispersive

effects. Revisiting the Navier-Stokes equation for laminar flow the body force term becomes the electrostatic Lorentz force $\left(\rho_E \vec{E}\right)$

$$\vec{\nabla} P = \mu \nabla^2 \vec{u} + \rho_E \vec{E} \tag{1.10}$$

Where $\rho_E = F \sum z_i c_i$ is the charge density and $\vec{E}$ is the electric field. In the case of a channel of circular cross section with the diffuse layer thickness (λ) small compared to the channel radius the velocity profile reduces to 1D and in the absence of a pressure gradient equation (1.10) can be solved giving the well known Helmholtz-Smoluchowski expression

$$u(r) = \frac{\epsilon_0 \epsilon_r \zeta}{\mu} \frac{d\phi}{dr} \tag{1.11}$$

where $E_z = -\frac{d\phi}{dr}$.

1.2.7 Microfluidic Applications

By scaling down fluid flows different aspects of the flow become important when compared to macroscale fluid mechanics. This is important because for microfluidic applications to be effective these differences should be understood and exploited in designing fluid manipulation and control strategies. If applications are treated as scaled down versions of their macro counterparts resultant solutions are inelegant at best and potentially inoperable [21].

Many microfluidic components have been developed to exploit the physical phenomena unique to the microscale and to improve upon macroscale processes. For instance, laminar flow can be used to stream line processes by combining multiple functions in a single step as seen in devices like T-Sensors and H-Filters [10, 17] where transport and separation are achieved concurrently. Accomplishing multiple tasks at

once is something microscale flows are especially good at [7], similarly running simultaneous assays through multiplexing is an achievable feat [28]. Several groups have exploited the increased influence of surface forces in microfluidics by using them to drive and manipulate flows [18, 29, 30]. The array of methods to manipulate and analyze fluids has expanded vastly leading to integrated lab-on-chip devices, so named for their ability to incorporate the functionality of entire labs onto one small chip.

Electrokinetic methods can also be exploited to perform species preconcentration, transport and electrophoretic separation [31]. Appropriate use of scaling factors is one of the key advantages to lab-on-chip devices. Steps that are distinct on the macro scale can be integrated seamlessly in microfluidics due to the dominant physical phenomena at that scale.

1.3 Nanofluidics

Nanofluidics is the diverse field of study involving transport in or around nanometer-sized objects (< 100 nm). High surface area to volume ratios and relatively fast diffusion makes physics at these scales inherently different from macroscopic phenomena. Nanofluidic transport is entirely dominated by interfacial effects and diffusion, distinguishing it from its close relative, microfluidics. Nanofluidics, while only recently having gained a name of its own has been implicit in many fields for decades. The broad range of disciplines spans both new and old including physiology, membrane science, soil science, colloid chemistry microengineering and surface sciences [32]. It was with the rise of micro total analysis systems that the term came into popular use [1, 25] as efforts to integrate numerous biochemical analysis steps onto a single chip inevitably lead to a drive for smaller and smaller elements, drawing many comparisons to the

miniaturization of embedded processors [10]. Many phenomena unique to this reduced scale have been harnessed to control molecules for nanofluidic transistors [33] and molecular sieves [34] leading to applications in sensing [25], separation, heat and mass transfer and preconcentration as well as an increased understanding of biomolecular and physiological processes [35].

From a practical standpoint, to facilitate the study and use of nanochannels there must be a macroscopic interface; this is achieved by integrating nanostructures with microfluidic systems. This integration creates a complex interplay of diffusion, electromigration and charge effects acting over different domains that superimpose at the interface providing some unique phenomena including exclusion-enrichment effects [36, 37] and semi-permeability [38]. These phenomena will be described in the subsequent sections. In microfluidics the objective is to exploit these phenomena and specifically for lab-on-chip applications these interfacial effects can be used to sieve or pre-concentrate samples [34].

1.3.1 Nanofluidics for Sieving

Use of porous networks for separating species can be traced back to the early 1900's where the chemical engineering community pioneered studies relating to physical filtration [34, 39]. While use of the phenomena was common it was not necessarily indicative of the level of understanding held over the fundamental physical processes at work. It was not until some key early works studying the transport within fine slits and capillaries that a more complete picture started to evolve. Pioneering work by Burgeen and Nakache explored flow in fine slits and found high electrokinetic retarding flows in channels with high Debye length to channel height ratio's giving some indication as to

the mechanism of permeation and rejection mechanisms [40]. To model porous membranes fine capillaries were adopted by Rice and Whitehead developing a linearized model of concentration and field distributions for low zeta potentials (< 25mV) [41]. Levine et al. extended the work of Rice and Whitehead by implementing an approximation to the Poisson-Boltzmann equation for high zeta-potentials providing an analytical approximation for more practical ranges (100-200 mV) [42]. In their work they presented the general expression for electroosmotic velocity in a fine capillary

$$u = \frac{\epsilon_0 \epsilon_r \zeta E_z}{\mu}\left(1 - \frac{\psi(r)}{\zeta}\right) \tag{1.12}$$

Where ζ is the zeta potential of the charged interface, $\psi(r)$ is the potential due to the electric double layer (EDL) and E_z is the externally applied field. Equation (1.12) intuitively illustrates the effect of increasing the Debye length to channel radius ratio (λ/r). As λ/r becomes appreciable the average potential across the channel, $\psi(r)$, increases resulting in a retarded fluid motion.

In developing the space charge model Gross and Osterle were the first to propose a general solution without resorting to the Debye-Huckel linearization of the Poisson-Boltzmann equation [43]. The model did not impose the same limiting restrictions as the previous models but did require numerical methods and was more complicated and computationally intensive. While these works do not specifically study the transport within nanochannels they are instrumental in establishing the groundwork for electrokinetic transport on microscales that lead to later efforts capable of modeling high Debye length to channel height ratios via area average models [44] and models capable of probing nanofluidic transport properties [45, 46].

1.3.2 Microfluidics Meets Nanofluidics

Coupling microfluidics with nanofluidics is a natural progression in the effort towards further miniaturization. At these reduced scales new transport modes and fluid manipulation schemes become accessible opening new opportunities for science and engineering. The complementary nature of the two realms is best illustrated in electrokinetic applications where microfluidic channels transport bulk flows via electroosmosis and ionic current is regulated within nanochannel junctions.

Understanding the phenomena is essential to provide effective and efficient strategies for manipulating mass and charge for eventual device application. The superposition of electric fields at the interface can lead to unique and complex phenomena like concentration polarization that can be used for species separation and concentration. These properties are relevant particularly in biomedicine where the capability of dealing with small sample sizes is especially important [25].

A key difficulty in analytically describing transport when approaching the nano scale is dealing with the interfacial effects that become increasingly dominant as the surface area to volume ratio increases [47]. Specifically, as channels are reduced in size the dimensions can become comparable to the length scale characterizing electrostatic interactions within the electric double layer (EDL). The electrostatic interactions between ions in solution and surface charges present on membrane or pore walls can cause highly asymmetric concentrations within these ionic channels as counter-ions move to neutralize the surface charge resulting in permselectivity or co-ion exclusion (see Figure 1-2). While only more recently finding application in microfluidics, this effect has been employed extensively in membrane science [48]. In the microfluidic

community studies utilizing integrated nanofluidic filters were among the first wave of devices to efficiently and effectively trap and manipulate samples.

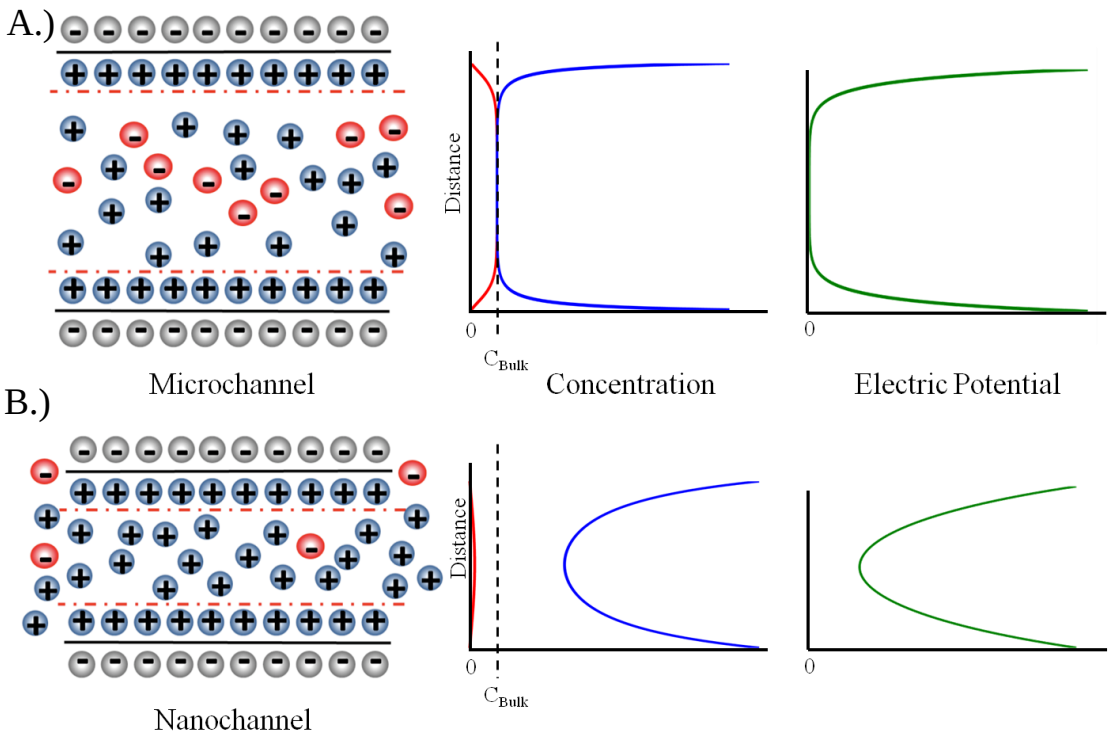

Figure 1-2| Surface charge effects in micro and nanochannels. **(A)** The EDL in a microchannel has a Debye length much smaller than the channel dimensions. The concentration in the microchannel is equal to the bulk solution concentration at the center of the channel. The electric potential decays rapidly leaving the bulk of the solution neutral. **(B)** In a nanochannel the solution is charged due to the interacting EDL's. The electric potential does not approach zero even at the center of the channel. The concentration distributions are asymmetric illustrating counter-ions are slightly higher in concentration compared to the bulk solution.

Kuo et al. integrated a membrane into a microfluidic device and modulated fluid flow through an externally applied bias across the nanofluidic interconnect [49]. Sample injection and collection were successfully demonstrated using the nanofluidic interconnects to transfer samples in a multilevel microfluidic architecture. Karnik et al.

demonstrated electrostatic control of ion concentration and conductance within nanochannels via gate electrodes [33]. The fluorescence intensity of negatively charged dye was monitored within the nanochannels as a gate voltage was applied. Negative voltage biases resulted in a reduction in fluorescent concentrations within the nanochannels while a positive bias increased concentrations.

In these earlier studies it was simply the transport of ions that was manipulated, however, from a lab-on-chip point of view it is often proteins that are of interest. Proteins are much larger and more complex than ions and interact with surfaces in a variety of ways, making control and manipulation more complicated. Karnik et al. was able to successfully demonstrated the field effect control of protein transport in using nanofluidic 'transistors' [50].

The surface charge effects being tuned and manipulated in these applications can also generate large concentration gradients between the anodic and cathodic micro/nano interfaces. This effect is known as concentration polarization.

1.3.3 Concentration Polarization

The observance of concentration polarization (CP) at micro/nano interfaces is a well-known phenomenon in membrane filtration processes where solvent concentrations, due to their exclusion from the membrane, rise on the feed side of the membrane. The resultant concentration gradient causes a potential in the opposite direction to the applied flux across the membrane [24, 51, 52]. In general the effect is associated with deleterious effects arising from the creation of depletion and enrichment layers with molecular diffusion boundary layers causing the local rise in osmotic pressure and limiting currents.

CP is a complex phenomenon and unlike many of the earlier studies mentioned that look at transport properties within single microchannels, CP requires a micro/nano interface. More recent efforts have looked at the propagation of CP from this interface [53, 54], an important parameter in applications using the effect as a method of increasing local concentrations in microfluidic applications.

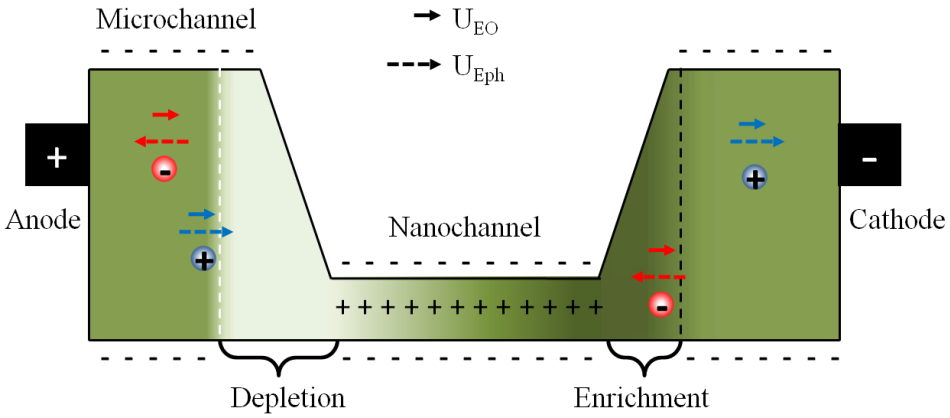

Figure 1-3| A microchannel in series with a nanochannel (negative surface charges) will exhibit asymmetric flux of cations and anions under the influence of an external field. The flux imbalance is caused by the exclusion of anions from the nanochannel region creating an enrichment region on the cathode side and a depletion region on the anode side.

Figure 1-3 illustrates some of the transport mechanisms at play at a micro/nanofluidic interface. The counter-ionic concentration is increased within the nanochannel to screen the surface charge thus excluding the co-ions. The resultant imbalance in flux creates an enriched zone on the cathodic side of a channel and a depleted region on the anodic side, otherwise known as the exclusion enrichment effect. In the depletion and enrichment zones, migration of cations and anions are in opposing directions developing concentration gradients. These gradients in turn lead to a flux of salt oriented toward the

nanochannel on the dilute (anodic) side and toward the bulk solution on the concentrated (cathodic) side.

The CP phenomena was qualitatively described by Pu et al. for the case of fabricated microchannel/nanochannel interfaces [36]. At electrochemical equilibrium a balance between chemical potential gradients and electrical potential generates an electrical phase boundary at the interface, a condition considered much earlier by Donnan for the case of two systems with different concentrations of fixed charge [55].

Plecis et al. gave a quantitative description of the permeability variance with ionic strength within a nanochannel structure [37]. Using reference parameters common to the membrane sciences the effective permeability (P_{eff}) was given as

$$P_{eff} = \frac{S_{eff} D}{L} = \frac{c}{c^*} S^* \frac{D}{L} \tag{1.13}$$

Where S^* is the geometrical section, D and L are the diffusion coefficient and length of the nanochannel, and c/c^* is the ratio of the concentrations with and without electrostatic interactions. The ratio c/c^* acts to effectively vary the sectional area increasing it for counter-ions and decreasing it for co-ions.

1.3.4 Analyte Concentration

At the reduced scale inherent with microfluidic technologies the sensing of target species can be difficult since the sample volume is reduced to nanolitres leading to low amounts of target analyte. This necessitates the need to preconcentrate samples prior to the sensing step. The exclusion-enrichment phenomenon associated with concentration polarization has been used within microfluidic platforms for the purpose of analyte concentration though methods have all been inherently 1-D, axial configurations [56-61].

Within this thesis an analyte concentration strategy based on a single microfluidic layer on a uniform nanoporous film is presented. As the active nanostructured region is defined by the microfluidics, this strategy provides flexibility and opens opportunities beyond the single-channel axial configurations to date. Radial geometries have not been previously shown operating as CP based concentration devices, though the unique geometry offers enhanced flux at the perimeter and the capability to focus samples down to small central regions. This focusing ability allows the concentration to take place on a separate layer and does not compete for space with other analysis fluidics. This radial configuration will be demonstrated within this thesis.

1.4 Continuum Assumption

The classic equations of fluid flow, mass transport and field distribution described herein rely upon the assumption of continuity. That is, the fluid and transport properties of interest such as density, viscosity, diffusivity, velocity, pressure, and temperature are assumed to be well-defined everywhere and are smooth functions in space and time. Such an assumption is well defined for systems with many molecules, though as the system scale is decreased the scarcity of molecules can create discrete effects not accounted for by the continuum approach. It is thus prudent to investigate the scale at which the continuum assumption breaks down. Qiao and Aluru provide a measure of the scale at which the continuum assumption can be applied by comparing the classical approach with molecular dynamic simulations [62]. Results indicate that continuum breaks down completely for liquids at dimensions less than 1 nm. Approximations are valid down to 2.2 nm though velocity profiles are generally overestimated due to the

observed increase in liquid viscosity near channel walls [62]. It is thus warranted to overestimate fluid viscosity within pores approaching this dimension.

In this thesis microstructures down to $20\,\mu m$ and a nanoporous membrane with 5 nm pores are modeled under the continuum assumption. While this approaches the limit of the assumption, satisfactory results have been obtained by others modeling transport with similar ion exchange membranes using continuum equations [63-65].

1.5 Overview of the Thesis

In this work the concentration polarization phenomena resulting at the interface of micro and nano structures is probed and used to concentrate analyte for potential application in diagnostics and electrophoretic separations. A device using a nanoporous membrane and microchannels to define the active micro/nano interface is developed and shown to be applicable to the concentration of protein molecules. The thesis is broken down into 5 chapters as follows.

In chapter 1 the aims and motivation were presented and a brief overview of relevant microfluidic and nanofluidic phenomena was discussed.

In chapter 2 a continuum based numerical model is developed for the study of concentration polarization in a micro/nano system. The effectiveness of a radial concentration device is investigated and the effect of field strength and particle mobility are investigated.

In chapter 3 the details of a radial device used to concentrate and focus analyte molecules are described. Experimental results for fluorescein and Bovine Serum Albumin (BSA) molecules are detailed and discussed.

In chapter 4 modified designs of the original concentrating device are presented, including a simplified fully planar method and a radial finned geometry. This approach aims to limit electrokinetic instabilities and further increase peak concentrations.

In chapter 5 the thesis is concluded with a look to potential future work stemming from the work presented here.

Chapter 2. Modeling the Concentration Polarization Phenomena

2.1 Introduction

In light of the recent interest in CP at micro/nanochannel interfaces there has been much work on developing nanochannel transport models accounting for embedded microchannels. Works include those based on the Poisson-Nernst-Planck (PNP) equations with simplified 1D models using porous materials [66] or 2D nanochannel simulations [67]. One-dimensional semi-analytical models based on the Poisson-Boltzmann equation also model micro-nano-micro channels with interacting EDL's [53, 68].

Plecis et al. developed a 1D model based on the PNP and Navier-Stokes equations to study the various modes of preconcentration [54]. For the purposes of preconcentration the highest concentration levels have been achieved with anodic stacking methods. This is due to the conductivity gradients that form on the cathodic side (enriched zone) which result in electric field gradients that can de-stack analytes [47].

Similar models using the PNP equations have been developed for 2D cases, Jin et al. developed such a model and demonstrated the buildup of a space charge region and vortical flows in the vicinity of a nanochannel/microchannel junction [67]. These models specify a constant surface charge density as one of the boundary conditions. Hughes et al. develop another model using a modified boundary condition based on the chemical equilibrium of hydrogen ions at the channel walls. This avoids the stipulation of the surface charge density which is often unknown, rather it is the pH which must be known, a quantity more readily accessible in the lab [69].

In an effort to avoid the numerical methods required to solve the strongly coupled and nonlinear PNP equations, Baldessari used the 1D Poisson-Boltzmann model to derive current and velocity properties of micro/nanochannel structures [68]. Mani et al. followed up with a similar model to study the propagation of the depletion region from the micro/nanochannel interface [53]. They characterized the necessary conditions for concentration 'shocks' (concentration differences at the bulk/depletion interface) to propagate and the velocity at which propagation occurs. Choi and Kim compared the two main modeling approaches, the PNP equations and the Poisson-Boltzmann method. They argued that the assumptions inherent in the Poisson-Boltzmann equation (namely that distributions were those at equilibrium) failed to accurately model overlapping EDL's, especially at lower ion concentrations where overlap would be significant. While the PNP model is more computationally intensive, results from experiments compared more favourably to this model [70]. There remains a lively debate on the issue.

Since all known experimental methods have been axial configurations such is true also of the aforementioned modeling efforts. Within this chapter a 1-D radial model is developed to explore the effectiveness of the proposed radial geometry in concentrating a target species.

2.2 Modeling Nanochannel Transport within a Nafion Nanoporous Membrane

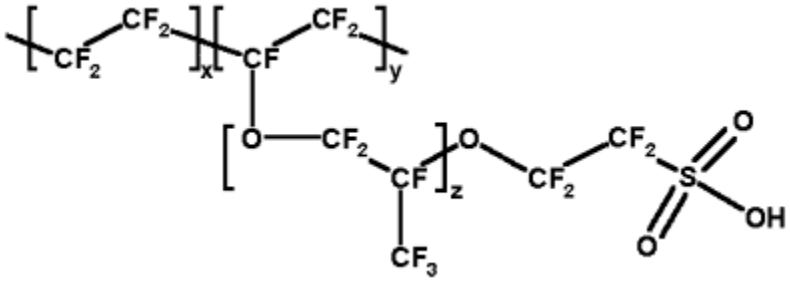

Figure 2-1| Chemical structure of H-form Nafion

Nafion is a perfluoronated sulfonic membrane composed of a fluorocarbon backbone and sulfonic acid groups SO_3H which dissociate into SO_3^- and H^+ in the presence of water (Figure 2-1). A hydrated Nafion membrane can be considered as a capillary network where the sulfonic groups are uniformly distributed at the pore surface giving a constant surface charge $\sigma_{surface}$ [65].

To model the electric double layer (EDL) the Stern-Gouy-Chapman model is adopted where the stern layer is taken as the effective pore boundary. This assumption necessitates the use of an effective surface charge σ where $\sigma < \sigma_{surface}$ since the positive charge in the Stern layer will screen some of the surface charge lowering its value at the outer Helmholtz plane [64, 65]. Within the literature various values of surface charge density exist varying from approximately -200mC/m^2 to -500mC/m^2 [65]. In the present model given the effective membrane conductivity is reduced at lower membrane thicknesses [63, 71] there is some uncertainty as to the value of σ. A value of -300mC/m^2 was found to provide a good fit to experimental data, was within the range of previously reported values and was applied in this work. Other parameters are

summarized in table 3 at the end of this chapter. It was assumed that the membrane hydration does not vary and the effect of varying water content on pore size is negligible. A constant radius of $r_p = 2.5\ nm$ was assumed [44, 72].

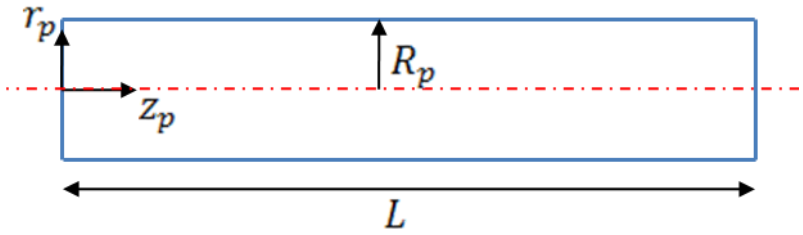

Figure 2-2| Schematic of the assumed cylindrical pore geometry employed in the computational model and the coordinate system.

First the equilibrium concentration and potential profiles within one pore (Figure 2-2) are established, the initial conditions for the membrane are then deduced by upscaling the model for a given porosity. The distribution of ions within the diffuse part of the double layer in a charged capillary is given by the Boltzmann distribution

$$c_i(z) = c_i^0 \exp\left(-\frac{\mathrm{z_i} e\psi(r_p, z_p)}{kT}\right) \tag{2.1}$$

Where e, k and T are the elementary charge, Boltzmann constant and temperature respectively. $\psi(r_p, z_p)$ is the field induced by the EDL and c_i^0 is the concentration where mathematically $\psi(r_p, z_p) = 0$.

To relate the channel potential with the variation in concentration, Poisson's equation is employed

$$\nabla^2 \psi(\mathrm{r_p}, \mathrm{z_p}) = -\frac{1}{\epsilon_0 \epsilon_r} \sum_{i=1}^{N} z_i F c_i \tag{2.2}$$

Expanding terms in the cylindrical coordinate system gives

$$\frac{1}{r_p}\frac{\partial}{\partial r_p}\left(r_p\frac{\partial \psi(\mathrm{r_p},\mathrm{z_p})}{\partial r_p}\right)+\frac{\partial^2 \psi(\mathrm{r_p},\mathrm{z_p})}{\partial {z_p}^2}=-\frac{1}{\epsilon_0\epsilon_r}\sum_{i=1}^{N} z_i F c_i \qquad (2.3)$$

where σ is the surface charge density $[C/m^2]$ and ϵ_r is the relative permittivity of hydrated Nafion which will be assumed constant and equal to 45 [73]. In long narrow capillaries ($L >> R_p$) the axial variation in potential is negligible compared with the radial variation and the axial derivative $\left(\frac{\partial^2}{\partial z^2}\right)$ can be neglected. Substituting the concentration distribution (2.1) into equation (2.3) gives the Poisson-Boltzmann equation

$$\frac{1}{r_p}\frac{\partial}{\partial r_p}\left(r_p\frac{\partial \psi}{\partial r_p}\right)=-\frac{1}{\epsilon_0\epsilon_r}\sum_{i=1}^{N} z_i F c_i^0 \exp\left(-\frac{\mathrm{z_i} e\psi}{kT}\right) \qquad (2.4)$$

Appropriate boundary conditions specify symmetry at the centerline (z = 0) and field flux at the charged surface

$$\begin{aligned} \frac{d\psi}{dr_p} &= 0, && r_p = 0 \\ \frac{d\psi}{dr_p} &= -\frac{\sigma}{\epsilon_0\epsilon_r}, && r_p = \mathrm{R_p} \end{aligned} \qquad (2.5)$$

Given the assumption of constant surface charge the model can be reduced to one dimension by taking area averages of potential and concentration distributions within the pores. The area average of a function within a cylindrical pore is defines as

$$\langle f \rangle = \frac{2}{{R_p}^2}\int_0^{R_p} f(r_p) r_p dr_p \qquad (2.6)$$

For the 1D model an expression is required to include the effect of surface charge (σ). In the 1D sense the effect is the same as a fixed charge concentration within the pore. Such

an expression can be obtained by integrating equation (2.3) with boundary conditions specified in (2.5)

$$\int_0^{R_p} \frac{\partial}{\partial r_p}\left(r_p \frac{\partial \psi}{\partial r_p}\right) dr_p = -\frac{F}{\epsilon_0 \epsilon_r} \sum_{i=1}^{N} z_i \int_0^{R_p} c_i \, r_p dr_p$$

Carrying out the integration yields

$$\frac{R_p \sigma}{\epsilon_0 \epsilon_r} - 0 = \frac{F}{\epsilon_0 \epsilon_r} \sum_{i=1}^{N} z_i \int_0^{R_p} c_i \, r_p dr_p$$

This reduces to an expression for overall electroneutrality

$$\sum_{i=1}^{N} z_i \langle c_i \rangle + \frac{2\sigma}{F R_p} = 0 \qquad (2.7)$$

The second term on the LHS of equation (2.7) can be thought of as the fixed charge concentration and is how the surface charge density enters the 1D model.

2.2.1 Summary of Initial Conditions

Equation (2.4) was solved numerically in Matlab using the BVP4C command to provide concentration and potential profile distributions (see Appendix A for calculation details). The potential at the wall (i.e. at the stern layer) was taken as the zeta potential (ζ) of the pore and used in subsequent pore velocity calculations. Results were subsequently numerically integrated using the trapezoidal method in accordance with equation (2.6) to obtain area average values. Only solution of the co-ion species concentration field is required while the condition of electroneutrality (equation (2.7)) is used to solve for the counter-ion distribution.

2.3 Hydrodynamics within Nanochannels

Under the influence of an applied field the electrostatic potential at any point in the problem domain can be decomposed into a linear superposition [24]

$$\Phi(\mathrm{r},\mathrm{z}) = \phi(z) + \psi(r,z) \tag{2.8}$$

Where $\phi(z)$ is the field due to an applied voltage and $\psi(r,z)$ is the potential due to the EDL. Newtonian laminar fluid flow with constant properties in a narrow cylindrical capillary is governed by the Navier-Stokes and continuity equations in cylindrical coordinates as follows

$$-\frac{\partial P}{\partial z} + \mu \frac{1}{r_p}\frac{\partial}{\partial r_p}\left(r_p \frac{\partial u}{\partial r_p}\right) - \sum_{i=1}^{N} z_i F c_i \frac{\partial \phi}{\partial z} = 0 \tag{2.9}$$

$$\frac{\partial u}{\partial r_p} = 0 \tag{2.10}$$

With boundary conditions

$$u(R_p) = 0; \qquad \left.\frac{\partial u}{\partial r_p}\right|_{r_p=0} = 0 \tag{2.11}$$

where P is the induced pressure required to maintain system continuity and μ is the viscosity assumed to be constant and equal to $1 \times 10^{-3}\, kg/m \cdot s$ within the pore. Equation (2.9) has the electrical body force included accounting for the effect of the externally applied electric field. To avoid solving the full Navier-Stokes equations the analytical solution to the velocity profile in a capillary will be used. The velocity profile is a linear superposition of electroosmotic and induced pressure driven flows, equations (1.8) and (1.12) [42, 74].

$$u(r_p) = -\frac{1}{4\mu}\frac{dP}{dz_p}\left({R_p}^2 - {r_p}^2\right) + \frac{\epsilon_0\epsilon_r\zeta}{\mu}\left(1 - \frac{\psi}{\zeta}\right)\frac{d\phi}{dz_p} \qquad (2.12)$$

The area average of this equation can be taken with the result

$$\langle u_p \rangle = -\frac{{R_p}^2}{8\mu}\frac{dP}{dz_p} + \frac{\epsilon_0\epsilon_r\zeta}{\mu}(1 - G)\frac{\partial\phi}{\partial z_p} \qquad (2.13)$$

where, as per Levine et al.[42] G is defined as

$$G = \frac{2}{\zeta {R_p}^2}\int_0^{\mathrm{Rp}} r_p\psi(r_p)dr_p \qquad (2.14)$$

The zeta potential is a function of the local concentration and thus will vary between the nanofluidic and microfluidic regimes. Additionally, the concentration at the interface between these two domains varies significantly on account of the exclusion enrichment effect. To facilitate numerical simulation of this dynamic process the factor $\zeta(1 - G)$ is calculated over a range of concentrations in the nano regime. Within the microchannel the factor $\frac{1}{\zeta h}\int_{-\frac{h}{2}}^{\frac{h}{2}}\psi(z)\,dz$ is calculated (see Table 3 for equations and domain details). Data can then be fit to a curve of the form [54]

$$\zeta_{Effectuve} = a_1\left(1 - \tanh\left(-\frac{\ln(\lambda(x))}{a_2} + a_3\right)\right) \qquad (2.15)$$

where pH is assumed constant and the Debye length (λ) has been introduced as the concentration dependent parameter. The resultant variation in the effective ζ with concentration can be seen in Figure 2-3 for the microchannel and nanopore.

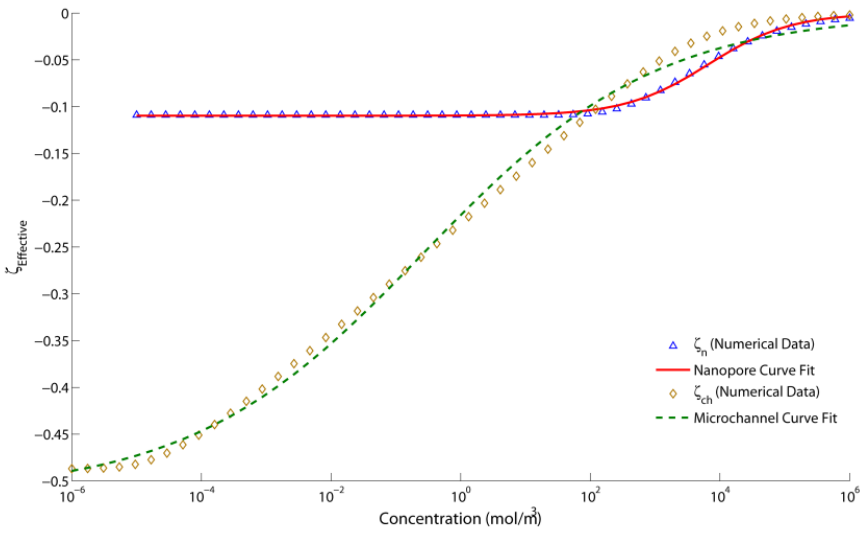

Figure 2-3| Effective zeta potential over a range of concentrations at T = 298K for $\sigma_{ch} = 150\ C/m^2$, $\sigma_m = 300\,C/m^2$, $h_m = 20\mu m$, $r_p = 2.5nm$

2.4 Species Transport

Within the microchannel domain, governing equations for the electric field and velocity profiles were developed as described in the previous section making careful note of the change in coordinate system. The overall problem domain (depicted in Figure 2-4) was approximated as two infinite parallel discs with varying height between the microchannel domain (h_{ch}) and membrane domain (h_m), here $h_{ch} = 20\mu m$ and $h_m = 50nm$. The variation in height and domain properties was modeled as a smoothed Heaviside function transitioning over a length of $5\mu m$. The $V_{Effective}$ boundary condtion at the central axis is of the form $V\left(1 - e^{-\frac{t}{0.65s}}\right)$, where the short time constant was added to avoid instabilities at the onset of the simulation.

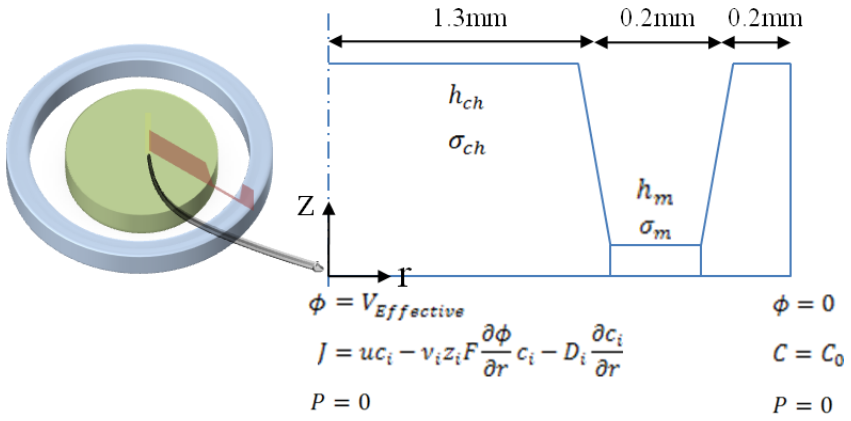

Figure 2-4| Overall problem domain. The surface charge and height properties vary from the micro domain to the channel domain, the transition is modeled as a smooth step over $5\mu m$. Boundary conditions at the outlet edge and channel edge are indicated.

An expression for species mass conservation within a dilute solution is given by the conservation equation

$$\frac{\partial c_i}{\partial t} + \nabla \cdot \mathrm{J_i} = 0 \tag{2.16}$$

where the species flux J_i is given by

$$J_i = uc_i - v_i z_i F \frac{\partial \phi}{\partial r} c_i - D_i \frac{\partial c_i}{\partial r} \tag{2.17}$$

where c_i, v_i, z_i, and D_i are the concentration, mobility, valence number and diffusion coefficient respectively for the i^{th} ion. F is Faraday's constant u and $\frac{\partial \phi}{\partial r}$ are the velocity and electric field strength respectively. Tabulated diffusion data was used to calculate the ion mobilites using the Nernst-Einstein relation $\left(v_i = \frac{D_i}{RT}\right)$.

A binary symmetric buffer is assumed providing two dominant ionic species (i = 1,2) along with a negatively charged tracer, or analyte of interest (i = 3). As per

Pennathur and Santiago [45] the dilute binary solution approximation is still valid for low concentrations of tracer species. Integrating the expression over the channel height

$$\int_{-\frac{h}{2}}^{\frac{h}{2}} J_i \, dz = \int_{-\frac{h}{2}}^{\frac{h}{2}} u_r \, c_i dz - \nu_i z_i F \frac{\partial \phi}{\partial r} \left(\int_{-\frac{h}{2}}^{\frac{h}{2}} c_i \, dz \right) - D_i \int_{-\frac{h}{2}}^{\frac{h}{2}} \frac{\partial c_i}{\partial r} dz \qquad (2.18)$$

In this reference frame the area average function is defined as

$$\langle g \rangle = \frac{1}{h} \int_{-\frac{h}{2}}^{\frac{h}{2}} g(r,z) dz \qquad (2.19)$$

Expressing (2.17) in terms of area averaged quantities

$$\langle J_i \rangle = h \langle u \rangle \langle c_i \rangle - \nu_i z_i F \frac{\partial \phi}{\partial r} h \langle c_i \rangle - D_i h \frac{\partial \langle c_i \rangle}{\partial r} \qquad (2.20)$$

Two simplifications have been made in equation (2.20), first the convective term has been simplified $\langle u c_i \rangle = \langle u \rangle \langle c_i \rangle$ which equates to neglecting axial dispersive terms [44]. The simplification is justified by the work of Bernardi and Verbrugge [72] who showed within a Nafion membrane the velocity is essentially constant. The second simplification is the diffusion term $\frac{\partial h \langle c_i \rangle}{\partial r} = h \frac{\partial \langle c_i \rangle}{\partial r}$. Again, this simplification is justified in the case that $\left| \frac{dh}{dr} \right| \ll 1$ which is the case here.

Poisson's equation is again used to relate the channel potential with the concentration distribution, in the modified coordinate system

$$\frac{1}{r} \frac{\partial}{\partial r} \left(r \frac{\partial \phi}{\partial r} \right) + \frac{\partial^2 \psi}{\partial z^2} = - \frac{\mathrm{F}}{\epsilon_0 \epsilon_r} \sum_{i=1}^{N} z_i c_i \qquad (2.21)$$

Taking the area average of (2.21) with boundary conditions

$$\frac{d\psi}{dz} = 0, \qquad z = 0$$
$$\frac{d\psi}{dz} = -\frac{\sigma_{ch}}{\epsilon_0 \epsilon_r}, \qquad z = \frac{\mathrm{h}}{2} \tag{2.22}$$

Results in

$$\frac{1}{r}\frac{\partial}{\partial r}\left(r\frac{\partial \phi}{\partial r}\right) = -\frac{\mathrm{F}}{\epsilon_0 \epsilon_r}\sum_{i=1}^{N} z_i \langle c_i \rangle + \frac{2\sigma_{ch}}{h_{ch} F} \tag{2.23}$$

Equation (2.23) relates the radial variation in concentration to the field strength.

2.5 Relations to Porous Domain

Concentration within a nanopore is related to the membrane concentration via the porosity ϵ_w. Likewise from continuity the velocity within a pore can be related to the superficial velocity, that is the velocity through the membrane assuming no porous structure existed. The expressions relating the microchannel domain with the membrane and pore domain are

$$c_m = \epsilon_w c_p,$$
$$q'_{ch} = u_{ch} h_{ch} = u_m h_m = q'_m \tag{2.24}$$
$$Q_m = Q_p \epsilon_w = u_p A_p \epsilon_w$$

where $c_m$and c_p are the concentrations in the pore and membrane respectively and u_{ch}, u_m and u_p are the velocities in the channel, membrane and pore respectively. q'_{ch}, q'_m, Q_m and Q_p are the per unit depth and total flow rates within the channel, membrane and pore. A_p is the cross sectional area of the cylindrical pore.

2.6 Summary of Model Properties

In this section the properties and final form of the equations implemented in the commercial multiphysics software Comsol 3.5 are detailed. Justification for the concentration values employed is also presented.

2.6.1 Electrolyte Properties

In the experimental section of this thesis (Chapter 3) 10mM TAE buffer at pH = 8.1 is used as the background electrolyte (BGE). 10 mM TAE consists of 20 mM of Tris base (pKa = 8.1), 10 mM of Acetic Acid (pKa = 4.8) and 0.25 mM of EDTA. EDTA is used to sequester divalent cations that may interfere with biological studies and will be neglected in the model. For a partially ionized univalent weak electrolyte in dilute solution the effective mobility (ν_{eff}) [75] is given by

$$\nu_{eff} = \alpha\nu \tag{2.25}$$

Where α is the degree of dissociation and ν is the fully ionized mobility.

The Henderson-Hasselbach equation applied to the acid dissociation equilibrium $HA \rightleftharpoons H^+ + A^-$ gives an indication as to the magnitude of α

$$pH = pKa + log\frac{[A^-]}{[HA]} \tag{2.26}$$

Where $[A^-]$ is the concentration of the conjugate base and $[HA]$ is the concentration of the acid. In the case of Acetic Acid $pKa \ll pH$ the ratio $\frac{[A^-]}{[HA]}$ is large and it can be assumed that the acid is in its fully ionized state ($\alpha = 1$). In the case of a base the equilibrium is $BH^+ \rightleftharpoons B + H^+$ and equation (2.26) is modified as follows

$$pH = pKa + log\frac{[B]}{[BH^+]} \tag{2.27}$$

For the case where $pH \approx pK_a$ as with the case of Tris base the ratio $\frac{[B]}{[BH^+]} \approx 1$ and equal parts base and conjugate base are present giving $\alpha = 0.5$. Concentrations of positive and negative ions can thus both be taken as 10mM (10mol/m^3).

2.6.2 Equations and Parameters

Tables 1-3 break down the model and present relevant domain equations, parameters and initial conditions.

Table 1: Simulation Parameters (T = 298K)

Parameter	**Microchannel**	**Membrane**
D^+ (m^2/s), Valence	0.39×10^{-9}, +1	$0.5(0.39 \times 10^{-9})$, +1
D^- (m^2/s), Valence	1.1×10^{-9}, -1	$0.5(1.1 \times 10^{-9})$, -1
D_{Tracer} (m^2/s), Valence	4.2×10^{-10}, -2	$0.5(4.2 \times 10^{-10})$, -2
Buffer reservoir concentration, mM	10	-
Tracer concentration, mM	5×10^{-3}	-
Surface charge density σ, mC/m^2	150	300
Porosity, ϵ_w	1	0.28
Permittivity	80	45
Viscosity $\mu, kg/m \cdot s$	1×10^{-3}	1×10^{-3}

Diffusion parameters for the Acetate ion (D^-) and Tris Base (D^+) are based on refs [76, 77]. The fluorescein tracer diffusion coefficient (D_{Tracer}) is based on ref. [78]. A factor of 0.5 was applied for the diffusion coefficients in the membrane to account for the tortuosity in the membrane. The value of surface charge density was taken by halving the Nafion surface charge density (effectively averaging surface charge of the top PDMS surface and bottom Nafion surface).

Table 2: Initial Conditions

Microchannel	**Membrane**
$c_i = c_0$	$c_2 = \epsilon c_p$ $c_1 = c_2 + \frac{2\epsilon_w \sigma}{F r_0}$
$\phi = 0$	$\phi = \epsilon_w \psi_p$
$P = 0$	$P = 0$

Table 3: Model Equations by Domain

Parameter	Microchannel	Membrane	Nanopore
ϕ	$\frac{1}{r}\frac{\partial}{\partial r}\left(r\frac{\partial \phi}{\partial r}\right) = -\frac{F}{\epsilon_0\epsilon_r}\sum_{i=1}^{N} z_i\langle c_i\rangle + \frac{2\sigma_{ch}}{h_{ch}F}$	$\frac{1}{r}\frac{\partial}{\partial r}\left(r\frac{\partial \phi}{\partial r}\right) = -\frac{F}{\epsilon_0\epsilon_r}\sum_{i=1}^{N} z_i\langle c_i\rangle + \frac{2\epsilon_w\sigma_{eff}}{{R_p}^2 F}$	–
u	$u_{ch} = \frac{1}{2\mu}\left(z^2 - \frac{h^2}{4}\right)\frac{dP}{dr} + \frac{\epsilon_0\epsilon_r\zeta}{\mu}\left(1 - \frac{\psi}{\zeta}\right)\frac{d\phi}{dr}$ $\langle u_{ch}\rangle = -\frac{h^2}{12\mu}\frac{dP}{dr} + \frac{\epsilon_0\epsilon_r\zeta}{\mu}(1 - G_{ch})\frac{d\phi}{dr}$ $G_{ch} = \frac{1}{\zeta h}\int_{-\frac{h}{2}}^{\frac{h}{2}}\psi(z)dz$	$\langle u_m\rangle = \epsilon_w\langle u_p\rangle A_p h_m$	$u_p = \frac{1}{r\mu}\left({R_p}^2 - {r_p}^2\right)\frac{dP}{dz_p} + \frac{\epsilon_0\epsilon_r\zeta}{4\pi\mu}\left(1 - \frac{\psi}{\zeta}\right)\frac{d\phi}{dz_p}$ $\langle u_p\rangle = \frac{{R_p}^2}{8\mu}\frac{dP}{dz_p} + \frac{\epsilon_0\epsilon_r\zeta}{4\mu}\left(1 - G_p\right)\frac{d\phi}{dz_p}$ $G_p = \frac{2}{\zeta {R_p}^2}\int_0^{R_p} r_p\psi(r_p)dr_p$
c_i	$\frac{d\langle c_i\rangle}{dt} + \nabla\cdot\langle J\rangle = 0$ $\langle J\rangle = h\langle u_{ch}\rangle\langle c_i\rangle - \nu_i z_i F\frac{d\phi}{dr}h\langle c_i\rangle - D_{i,ch}\,h\frac{d\langle c_i\rangle}{dr}$	$\frac{d\langle c_i\rangle}{dt} + \nabla\cdot\langle J\rangle = 0$ $\langle J\rangle = h\langle u_m\rangle\langle c_i\rangle - \nu_i z_i F\frac{d\phi}{dr}h\langle c_i\rangle - D_{i,m}\,h\frac{d\langle c_i\rangle}{dr}$	$\frac{1}{r_p}\frac{\partial}{\partial r_p}\left(r_p\frac{\partial \psi}{\partial r_p}\right) = -\frac{1}{\epsilon_0\epsilon_r}\sum_{i=1}^{N} z_i F c_i^0 \exp\left(-\frac{\mathrm{z_i} e\psi}{kT}\right)$
P	$\nabla\cdot\langle u_{ch}\rangle = 0$	$\nabla\cdot\langle u_m\rangle = 0$	–

2.7 Results and Discussion

Numerical calculations were performed on a PC with an Intel Core i7 920 @ 2.67GHz processor and 12GB of RAM. The running conditions correspond to the experimental conditions as will be described in Chapter 3. The mesh consisted of 6787 elements with points being clustered at the interfaces of the micro and nano domains. Under these conditions solutions typically took between $5\frac{1}{2} - 6$ hours for 30 seconds of data. Of primary concern was the magnitude of the preconcentration effect and the time in which the sample can be concentrated. Peak concentration values with time were monitored for subsequent comparison with experimental data.

Figure 2-5 shows the evolution of the depletion zone and the resultant rise in tracer concentration as calculated by the numerical model. Here the 1D data from the model has been rotated about the center axis 360^0 to create a 2D plot facilitating comparison with the 2D experimental data.

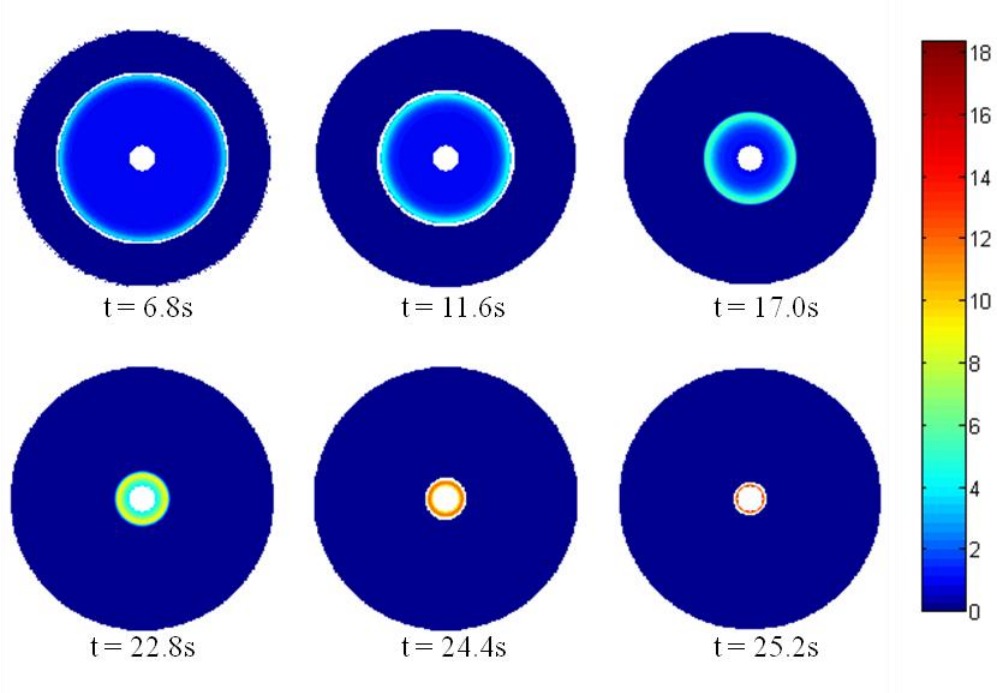

Figure 2-5| Radial preconcentration modeling results for 10mM TAE buffer and 5μM fluresceintracer. Focusing chamber diameter is 2.6mm, $h_{ch} = 20\mu m$, $h_m = 50nm$ and $V_{Effective} = 95\left(1 - exp\left(-\frac{t}{0.65s}\right)\right) V$

The build up of fluorescein at the depletion boundary as shown in the figure results in a maximum concentration increase of $18.32\times$ before the sample exits the central outlet outside of the computational domain**.** Figure 2-6 illustrates the time evolution of the peak dimensionless concentration $C^* = c_i/C_0$ showing the maximum concentration is reached in 25.6 seconds. The most notable distinction between these radial results and similar experimentally reported curves [59-61] is the highly non-linear nature of the concentration enhancement particularly at the later stages. In the axial instances previously sited the concentrations increase linearly initially and generally plateau at longer times (this plateauing is often attributed to increased protein adsorption rates at elevated concentrations [60]). In this radial case the concentration ramps up considerably

between 20 s and 25.6 s, this is due to the depletion interface corralling the sample and focusing it down to a small central area. The reduction in area is unique to the radial case and offers a distinct advantage when it comes to enhancing concentrations.

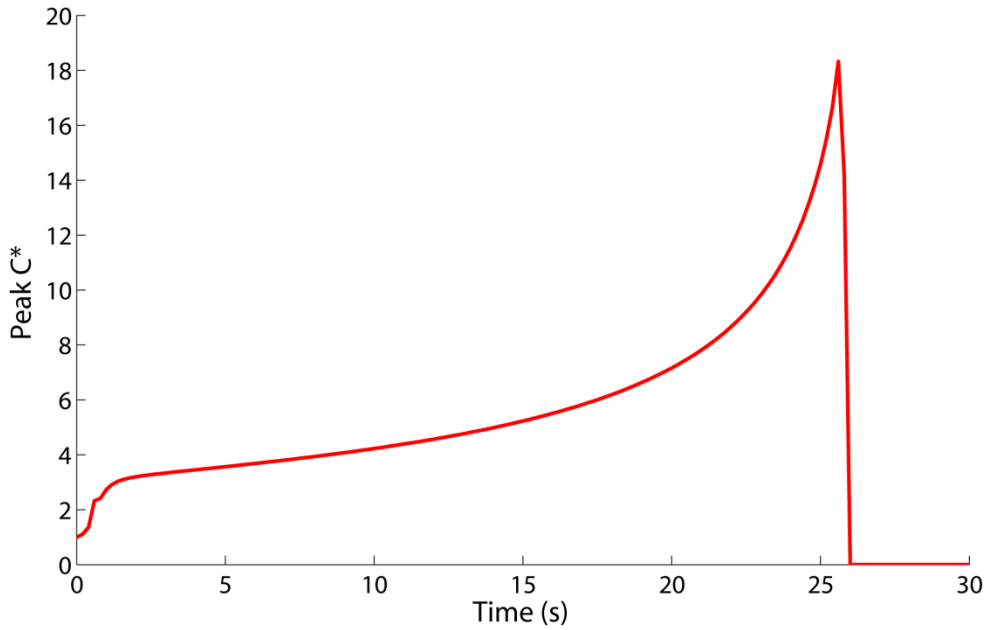

Figure 2-6| Evolution of peak concentration with time for the radial model. A maximum concentration enhancement of 18.32 × is achieved at 25.6 seconds.

2.7.1 Accumulation Rates

With the results of Figure 5 and 6, the calculated concentration rate can be compared to existing preconcentration methods in the literature. Taking the accumulation rate (R_{acc}) as

$$R_{acc} = \frac{C^*}{t_{acc}} \tag{2.28}$$

Where t_{acc} is the accumulation time in seconds. The maximum C^* value obtained here for fluorescein is 18.32 in 25.6 seconds, this corresponds to an $R_{acc} = 0.7\frac{1}{s}$.

Wang et al. first reported million-fold concentration enhancement in 2005 using the exclusion enrichment effect [60]. They reported concentration enhancements of Green Fluorecent Protein (GFP) of 10^7 within 1 h giving an $R_{acc} = 2{,}777\frac{1}{s}$.

Using Nafion junctions Lee et al. [59] increased the concentration of β-PE protein by a factor 2×10^4 within 5 minutes representing an $R_{acc} = 66.7\frac{1}{s}$. Likewise Kim and Han [56] using vertical Nafion junctions concentrated the same protein by a factor of 10^4 within 22 min. giving $R_{acc} = 7.6\frac{1}{s}$.

The highest reported accumulation rates that could be found presently were those reported by Wu and Steckl [61] who concentrated FITC-HSA proteins at the interface of a polycarbonate track etched membrane. R_{acc} values of $5,000\frac{1}{s}$ over 200s were reported though peak concentrations were accumulated over a very small area of the $50\ \mu m \times 50\ \mu m$ membrane.

The accumulation value reported here is significantly lower than some reported values, however concentration rates are highly dependent upon ion and molecule mobilities and applied voltage. Given that a small mobile molecule like fluorescein was used in the initial trials with relatively low effective voltages (< 100V) the effects of modifying these parameters (voltage and mobility) will be investigated in the next sections through modeling simulations.

2.7.2 Preconcentration Rate Enhancement

Development of the depletion zone is limited by how fast the ions can vacate the depleted region. The interface between the depleted region and the bulk solution is characterized by a large conductivity gradient which gives rise to an extremely large field gradient [79],

thus referencing equation (2.20) we can say that the electrophoretic term dominates the flux and the equation reduces to

$$\langle J \rangle \approx -\nu_i z_i F \frac{\partial \langle \phi \rangle}{\partial r} h \langle c_i \rangle \tag{2.29}$$

Where it is seen that for an applied field and channel height the flux and thus evolution of the depletion zone is increased by increasing the ion mobility. If high mobility ions such as Na^+ and Cl^- are added to the buffer solution the effective mobilities of the co-ions and counter-ions would increase. Increasing the mobilities two-fold over the conditions in Figure 2-6 vastly improves the performance of the concentration device as illustrated in Figure 2-7.

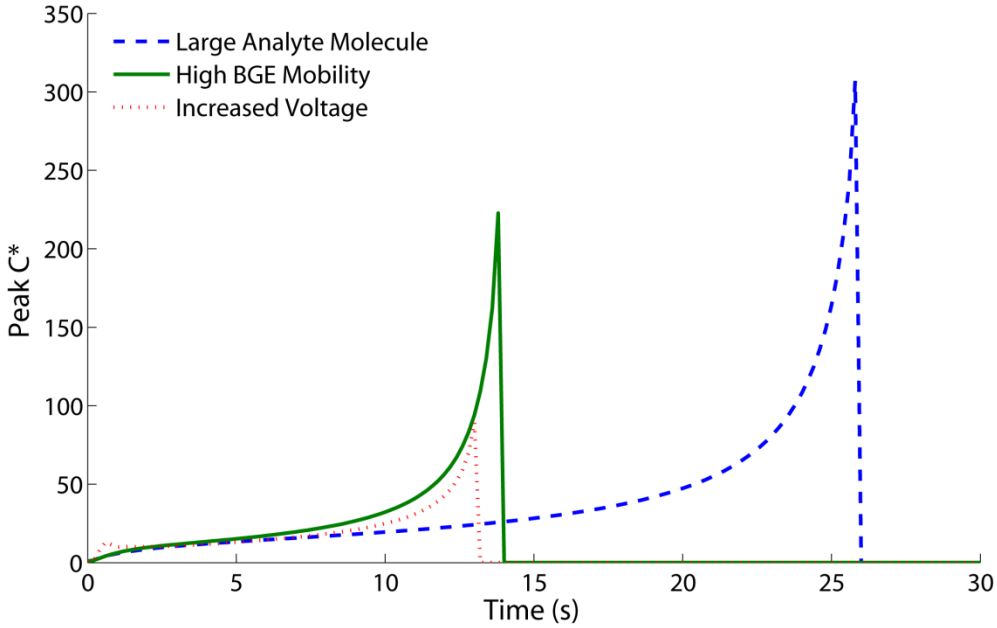

Figure 2-7| Peak C^* with time under various optimizing conditions. (High BGE Mobility) Increase in diffusion coefficients to $D^- = 1.8 \times 10^{-9}\, m^2/s$ and $D^+ = 0.8 \times 10^{-9}\, m^2/s$. A rise in peak concentration and a reduction in time are seen over the previous case with reduced mobilities. (Large Analyte Molecule) An analyte molecule with $D = 6.1 \times 10^{-11}\, m^2/s$ and $z = -10$. An increase in the preconcentration efficiency is seen as more molecules are effectively trapped at

the depletion interface. (Increased Voltage) An effective voltage of 200V is applied reducing the concentrations time and moderately improving the maximum concentration factor.

For increased mobilities BGE ion diffusion coefficients were increased to $D^- = 1.8 \times 10^{-9}\, m^2/s$ and $D^+ = 0.8 \times 10^{-9}\, m^2/s$. A peak C^* of 222.8 is reached in 13.8s giving an $R_{acc} = 16.1\frac{1}{s}$, a vast improvement. While still not in league with values of 2000 – 5000, of note is the time required, less than 15 seconds. The vast majority of accumulation is accomplished within the last 2 s, unlike traditional linear schemes the radial configuration produces a highly non-linear accumulation rate. Within the first 12s $R_{acc} = 4.7\frac{1}{s}$ while in the last 1.8 s $R_{acc} = 92.4\frac{1}{s}$.

Alternatively, a benefit in accumulation rate can be obtained by modifying the analyte mobility (and keeping the original BGE mobilities). In this case since negatively charged molecules are being used it's desired to reduce the flux of the analyte, in this manner the depletion zone will evolve much faster than the analyte and effectively corral more of the sample. Proteins are much larger and slower than fluorescein molecules, taking values for Bovine Serum Albumin (BSA) at pH = 8.1 z = -10 and $D = 6.1 \times 10^{-11}\, m^2/s$ [80]. Figure 2-7 shows the improvement in peak concentration for this scenario (blue dashed line). The simulated time remains the same at 25.8s but the concentration factor reaches a maximum of $C^* = 307$ giving an $R_{acc} = 11.9\frac{1}{s}$. There are other concerns surrounding proteins including the variance of shape and charge with pH and the tendency to adsorb onto surfaces that will be looked at in Chapter 3.

The final variable investigated is the effective voltage. Increasing this variable should again increase the flux and thus faster preconcentration rates are expected which as

Figure 2-7 (red dotted line) illustrates this is the case with an $R_{acc} = 6.8\frac{1}{s}$ for $V_{Effective} = 200V$. Of note is that while increasing the voltage has a large effect on the concentration time there is not as notable an effect on the maximum concentration factor attained. This is to be expected since the applied voltage has a universal effect, that is, all ions including BGE and analyte molecules experience the increased flux. Additionally the increased flux is felt throughout the microchannel causing higher sample losses at the outlet as compared to when just mobility values are altered.

The effect of varying multiple parameters on peak C^* is demonstrated in Figure 2-8 where all three parameters are adjusted (Optimized Conditions line) to conditions established in Figure 2-7 and just the mobilites are adjusted (Optimized Mobilities). The term 'optimized' is used here in the sense that the following parameters were adjusted to achieve maximum peak concentration values assuming the large molecule: $V_{Effective}$, D^+, D^-. While this optimization is rough as compared to formal, global optimization, the results provide an indication of the performance levels that can be expected. Specifically, the accumulation rates for both cases are $R_{acc} = 252.2$ and $R_{acc} = 75.7$. It is seen that this method works best for bigger molecules in high conductivity solutions at high voltages. Under these optimized or ideal conditions significant improvements are seen in terms of both time and concentration levels. If these values could be realized in practice the method would provide the rates and times necessary with the added benefits of ease of use and fabrication. Additionally, the method affords the integration of the concentrating chip in a secondary layer since concentrated plugs can be focused to central regions and ejected.

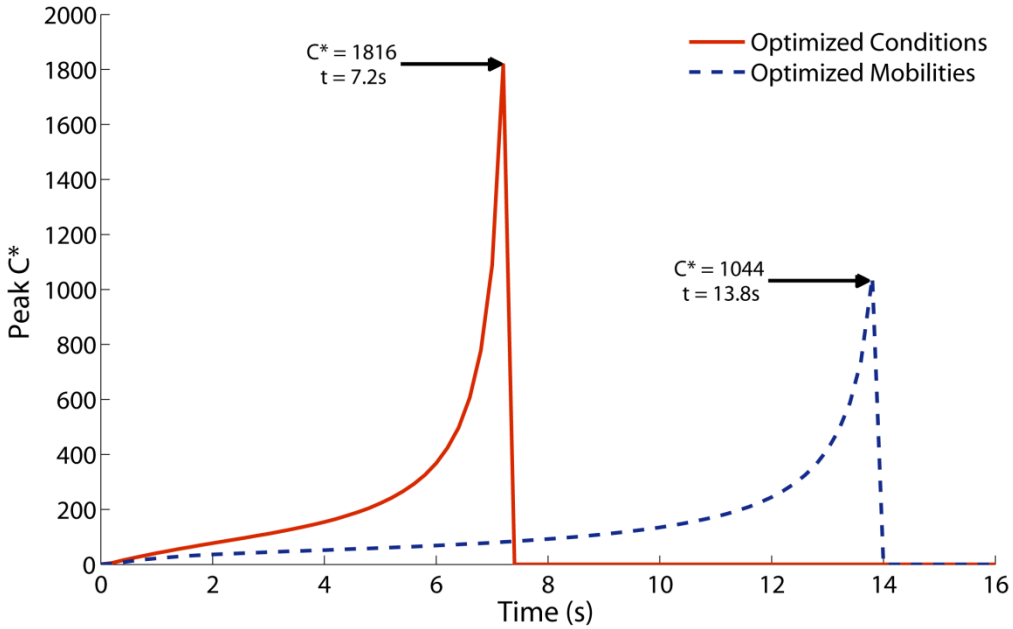

Figure 2-8| Simulated results for optimized variables. (Optimized Conditions) The BGE mobilites, analyte mobility and effective voltage have all been optimized, the resultant peak concentration is the highest seen at 1816 and the fastest at 7.2s. (Optimized Mobilites) By optimizing the BGE and analyte mobilities a significant improvement in peak concentration is seen.

The simulations help demonstrate the proof-of-concept operation for the radial concentration scheme, and indicate that the running parameters have a large effect on the preconcentrations effectiveness. In practice the BGE mobility and effective voltage may not attain the simulated values due to the onset of electrokinetic instabilities [81-83]. These instabilities are discussed in Chapter 4 and a potential solution is demonstrated.

2.8 Summary

This chapter described the model used for nanofluidic transport within highly charged nanopores. Concentration and potential distributions along with velocity profiles were

detailed for a nanopore and scaled up to provide properties within a thin nanoporous membrane region. The problem was further scaled up to a micro-nano-micro radial domain and the concentration polarization phenomena at the micro-nano interface was demonstrated. It was seen in the results that the propagation of the depletion zone was an unsteady process that could be used to corral slower analyte molecules at the depletion interface producing a concentration enrichment effect. Factors effecting the concentration enhancement such as the electric field strength, BGE ion mobilities and analyte ion mobility were studied. Concentration enrichment rates of $75.7\frac{1}{s}$ and $252.2\frac{1}{s}$ were predicted for larger molecules ($D = 6.1 \times 10^{-11}, z = -10$) and high mobility BGE solutions ($D^+ = 0.8 \times 10^{-9}\frac{m^2}{s}, D^- = 1.8 \times 10^{-9}\frac{m^2}{s}$) at moderate (95V) and high (200V) potentials. Importantly, these results demonstrate proof-of-concept operation of a radial analyte concentration scheme. This is the first work in this area as all other concentration schemes have been 1-D axial within a channel. The results indicate that the technique shows promise and could provide certain advantages in terms of on-chip integration, ease of use and chip-area required. Experimental testing and subsequent comparison with the numerically predicted results are required to assess the technology, and these aspects are the focus of Chapters 3 and 4.

Chapter 3. Concentration with Nanoporous Films and Radial Microfluidic Structures

3.1 Introduction

Changing protein expression profiles within biological fluids can be indicators of many diseases [84]. Measurement and identification of such proteins is thus a vital tool for medical diagnostics. A challenge to sensing these changes comes from the large dynamic range of protein concentrations within plasma, spanning 10 orders of magnitude with many potential biomarkers in the lower ranges [85]. These low abundance proteins require pre-concentration steps and the use of traditional immunoassay and liquid mass spectrometry methods are still time consuming and challenging processes for detecting target species [86, 87].

Microfluidic methods have emerged as platform technology for automated, high throughput biomolecular analysis, allowing various separation, concentration and detection steps to be performed on a single integrated microfluidic chip [88]. At the reduced scale inherent with microfluidic technologies the concentration step is even more important since the sample volume is reduced to the nL scale leading to low amounts of target analyte. To date there exist a number of effective preconcentration strategies that exploit the concentration polarization phenomena occurring at the interface between micro and nano structures in the presence of an applied electric field.

Pioneering preconcentration efforts in microfluidics utilized nanoporous networks in track etched membranes [36, 49], and fabricated nanofluidic channels [36, 89]. Wang et al. demonstrated concentration factors of rGFP as high as 10^6 – 10^8 using 40 nm channels in times of 40 minutes to 3 hours [60]. The method relied upon the balancing of

fields tangential (E_T) and normal (E_n) to the nano/micro interface. When the ratio of the tangential and normal electrical fields (E_T/E_n) is optimized the depletion interface is stabilized and ions can be accumulated over the long durations mentioned. Application of the tangential field in this method does make it susceptible to secondary electroosmotic flows which can cause mixing and destroy depletion layers [79].

To alleviate the requirement for nanofabrication, nanoporous media have been used including gels [66, 90], and more recently cation selective membranes such as Nafion [56, 58]. In a series of papers, Han's group used Nafion as a planar or vertical nanofluidic junction connecting microchannels to achieve easily fabricated preconcentration devices [56, 58, 59]. Experiments were able to continuously accumulate charged proteins from a 1-10 μL sample and confine them to a volume of 1 pL to 1 nL at the interface of the depletion region.

More recently Wu and Steckl achieved impressive concentration rates using a multilayered chip and PCTE membrane (10 nm pores) similar to what Kuo et al. used to gate flow across a nanofluidic interconnect [91]. Protein accumulation factors of ~10^5 – 10^6 were achieved within only 200s [61]. All known CP based preconcentration efforts have been inherently 1-dimensional, accumulating molecules within 1d axial channels.

In this chapter a planar Nafion membrane is used in conjunction with novel radial channel geometries. The proposed radial concentration method has the following advantages:

1) The use of radial geometries allows the non-linear interfacial effects to confine and focus samples to small central regions

2) The layout is amenable to coupling with integrated microsystems since larger initial volumes are focused and can be injected into secondary analysis layers
3) The multidimensional process leads to an increased interfacial area and increased ionic currents
4) No flow balancing via pressure driven flows is required and no optimum ratio of tangential and normal electric fields need be obtained, as compared to previous concentration schemes [56-61]
5) Fabrication procedures are planar and use standard soft lithography with the only additional step required being the spin coating of a Nafion membrane, that is, simple microfluidic-scale fabrication may be used to define the effective geometry of the nanoporous membrane
6) Since the entire bottom substrate of the chip assembly is coated with the membrane, issues associated with patterning and bonding of intermediate membrane layers is avoided

The effectiveness of the radial configuration will be experimentally verified in this chapter.

3.2 Experimental

3.2.1 Materials and Device Fabrication

Tris-Acetate EDTA (TAE) buffer at 0.25X (10 *mM*, pH = 8.1) was used as the background electrolyte for all experiments. Fluorescein isothiocyanate labeled bovine serum albumin (FITC-BSA) (Sigma Aldrich, St. Louis, MO) and fluorescein (Invitrogen Inc., ON) were used as the target analytes.

The microfluidic chip was fabricated in poly-dimethylsiloxane (PDMS) (Sylgard, Dow Corning Corporation, Midland, MI) using established soft-lithography techniques. [92, 93]. Inlet and outlet holes were punched in the PDMS at the reservoir locations, an additional small diameter hole was punched at the center of the circular chamber using a 25 gauge needle (ID = $241.3\mu m$) with the end ground flat. For protein trials the PDMS chip was washed with isopropyl alcohol and dried prior to being sonicated in a 1% water/tween-20 solution for 30 minutes to reduce protein surface adsorption to the PDMS surfaces (no treatment in tween-20 solution was carried out for fluorescein trials). Following this the chip was treated in a Plasma Cleaner (Harrick PDC 32-G) for 60s to ensure a hydrophilic surface. The chip was then brought into contact with a Nafion coated substrate and clamped between two PMMA plates, Figure 3-1 shows the assembly of the microfluidic chip. For difficult geometries a drop of the working solution was placed on the Nafion prior to placing the PDMS chip on top, this allowed the fluid to fill difficult spaces, assembly then commenced as normal. Any entrapped air bubbles were removed using the vacuum assisted filling techniques detailed in Ref. [94]. Once filled chips sat for a minimum of 20 minutes to allow the Nafion to hydrate.

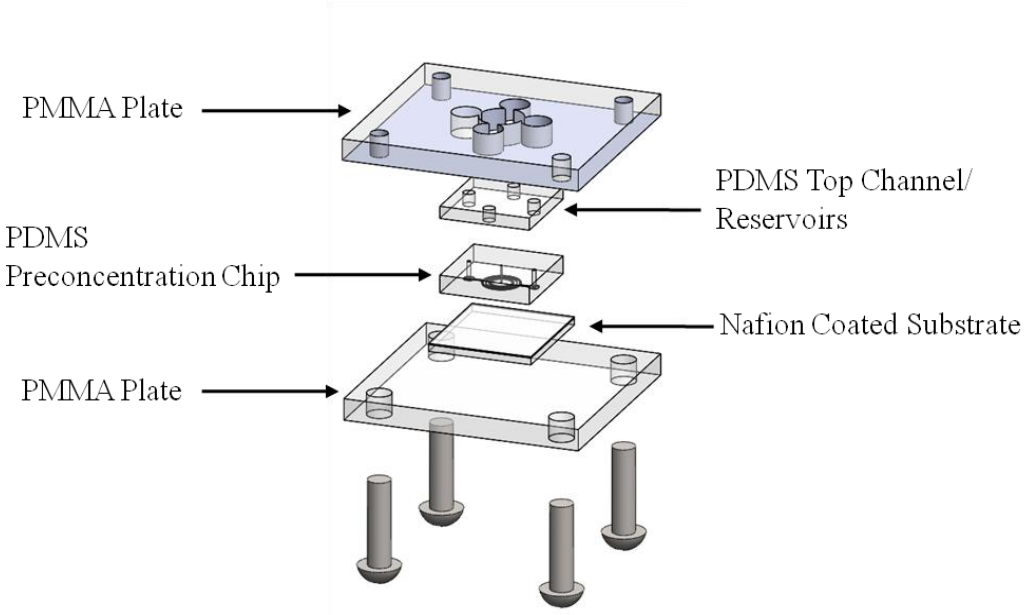

Figure 3-1| Chip Assembly

To fabricate the substrate a PDMS coated glass slide was plasma cleaned to render the surface hydrophilic. Following the plasma treatment $400\mu L$ of a solution of 5% Nafion 117 in a mixture of lower aliphatic alcohols (Sigma Aldrich, St. Louis, MO) was spin-coated onto the PDMS coated glass slide at 680 rpm for 30 seconds. To allow the solvent to fully evaporate the coated slide was left for a minimum 48 hours at room temperature prior to use.

3.2.2 Microfluidic Chips

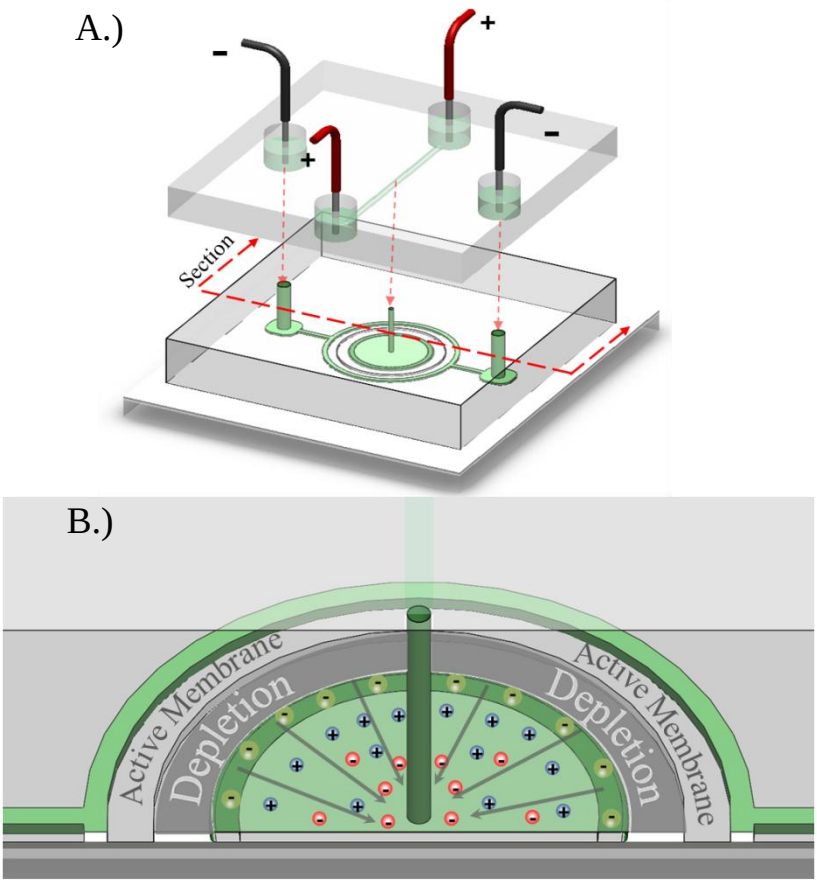

Figure 3-2| **(A)** Schematic of microfluidic preconcentration device. The central radial chamber on the bottom layer concentrates analyte via application of electric fields as indicated. **(B)** A magnified cross section of the radial chamber where preconcentration takes place. Upon application of an external electric field a depletion zone forms at the microfluidic/nanofluidic interface. The evolving depletion zone causes a build-up of analyte molecules at the interface with the bulk sample. As time increases the depletion region focuses analyte molecules to the centre and injects them into the secondary layer**.**

Electric fields were applied via two positive and two grounded platinum electrodes in the reservoirs, as shown in figure 3-2A. The top PDMS layer contains the electrode reservoirs and a straight channel that could be used for separation of concentrated analyte. The bottom PDMS layer contains the radial preconcentration chamber and an outer grounded channel network. The radial concentration polarization dynamics for a

negatively charged nanporous film (Nafion) is illustrated in figure 3-2B. Under the influence of an applied electric field the cation selectivity of the Nafion membrane creates an enrichment effect on the cathode side and a depletion effect on the anode side. Due to the highly charged nature of the Nafion membrane the depletion layer does not reach steady state and its evolution is used to corral analyte molecules at the interface of the depletion region and focus them into the injection point.

3.2.3 Data Acquisition and Analysis

An inverted fluorescence microscope (DMI 6000B, Leica , NJ) was used to image tracer transport and accumulation. Image sequences were captured using a CCD camera (Orca AG, Hamamatsu, NJ) installed on the microscope, and the images were imported into ImageJ (free software) for image processing. To normalize the fluorescence images, a dark field image was subtracted and bright field normalization was performed according to

$$C^* = \frac{C_{raw} - C_{dark}}{C_{bright} - C_{dark}} \tag{3.1}$$

Images were then smoothed with a mean averaging filter using a square kernel between 5 and 8 pixels. Following the normalization procedure images were imported to MatLab (Mathworks Inc.) for quantification. Normalized pixel intensity values were scaled to fill the output range and false colour maps of concentration were generated directly from this normalized data. Average peak values were measured over the region of interest which encompassed the radial focusing chamber.

3.3 Results and Discussion

3.3.1 Fluorescein Concentration Trials

The preconcentration effect for fluorescein analyte molecules is shown in the intensity plots of Figure 3-3 at varying stages of progression. At t = 6.5 s the onset of depletion is observed at the left and right hand borders of the focusing chamber. The continued evolution of this depletion region (t = 24.5 s and t = 26.0 s) corrals the analyte creating concentration spikes at the interface of the bulk and depletion region. As the analyte is focused down to the small central region at t = 27.0 s the maximum concentration of $18.95\times$ is attained. The last time step at t = 33.0 s shows the concentrated plug being injected into the upper analysis channel. The applied voltage in this case is 400V though the effective voltage difference across the channel will be less than this due to losses through the top channel and grounding channels. Some asymmetry in the concentration profiles result, mainly due to the use of only two grounding channels at the left and right hand sides of the focusing chamber (not shown). This explains why the initial depletion develops in these regions and will affect the symmetry throughout.

Within the current electrode scheme rather than being pinched at the outlet the sample is seen to disperse and split in two once ejected into the top channel. It can be seen from the zeta potentials in figure 2-3 that the flow rate induced in the nanopores is less than the flow rate in the microchannel due to the high electro-viscous retarding forces seen in channels where dimensions approach the Debye length. The result is an induced back pressure at the micro-nano interface that builds with time creating a pressure driven component to the flow field [54]. Once the concentrated plug reaches the outlet the induced pressure driven flow drives the plug in the upper channel causing the

typical dispersive effects associated with pressure driven flows. To avoid these secondary pressure driven flows a voltage switching scheme could be implemented to remove the ground electrodes once the analyte has been focused into the outlet. Removing the ground electrodes eliminates the electroosmotic bulk flow that produces the back pressure.

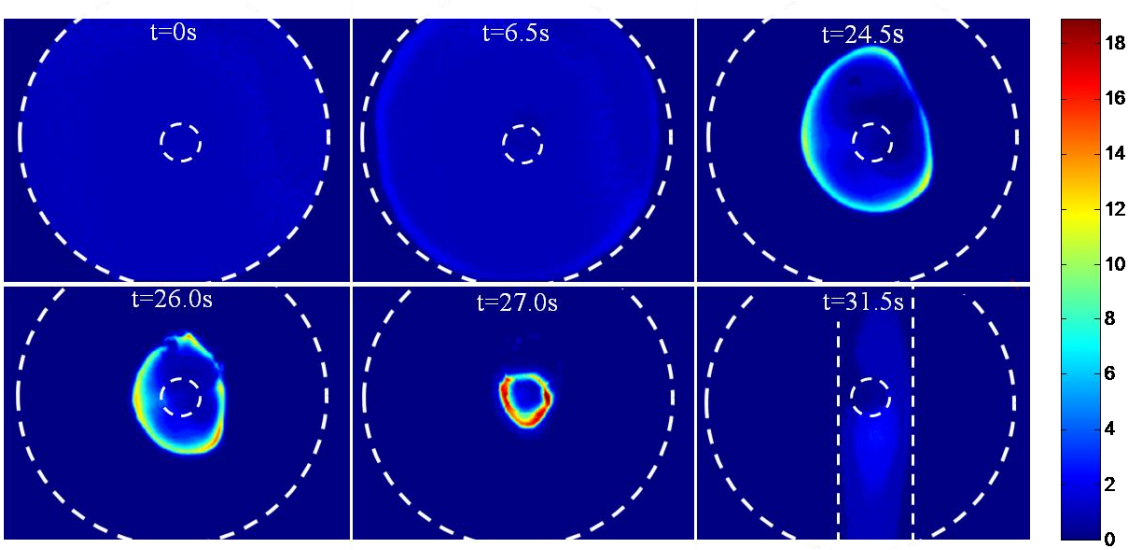

Figure 3-3| Concentration profiles of 5 μM fluorescein in 10 mM TAE buffer at $V_{applied} = 400\,V$. $h_{ch} = 20\mu m$, focusing reservoir (white dashed outline) diameter = 2.6 mm. A peak concentration enhancement of 18.95 X is obtained in 27.0 s.

3.3.2 Comparison with Numerical Model

Figure 3-4 compares the model and experimental results for the time evolution of peak C^*. The model closely fits the trend of the experimental data with some deviation from the experimental data at the beginning and end of the simulation attributed partly to the addition of the time constant in the voltage boundary condition. Also, there will be some variation in effective voltage as the depletion region evolves and the outlet flux will likely vary in the experimental case due to the method of fabricating the central hole. The hole must be punched and will be slightly off center and while it is approximated as

200 μm in diameter the punching method creates a tapered exit hole larger than 200 μm. Other variances can be attributed to assumptions of constant temperature, constant viscosity and a binary electrolyte solution. In practice NaOH is often added to TAE to bring the pH up to working conditions. The addition of sodium ions and the uncertainty of the contribution of H^+ ions within the Nafion will affect ion mobilities. Some of these errors will be absorbed into the property values used for the Nafion film since they were used as fitting parameters. The small rise in concentration at the 32 second mark for the experimental data is due to the concentrated plug exiting the outlet hole and traveling through an upper channel.

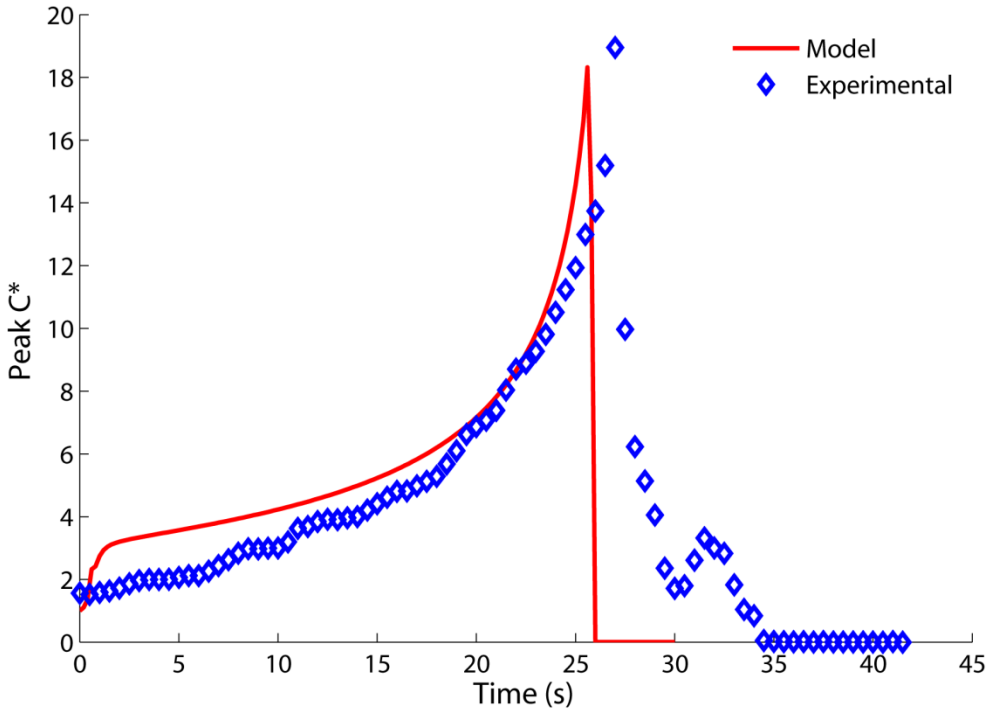

Figure 3-4| Comparison of experimental and modeling data.

An advantage of this radial configuration, as compared to previous concentration schemes [56-61] is that no flow balancing via pressure driven flows is required and no

optimum ratio of tangential and normal electric fields need be obtained. All that is required is that the BGE ion mobilities be higher than the target molecules mobility, the higher this ratio the greater the collection efficiency as indicated in Chapter 2. In practice increasing the BGE conductivity (thus ion mobility) or increasing voltages often resulted in unstable depletion interfaces that gave unpredictable and irreproducible results. To attain higher concentration factors Chapter 4 will look at potential solutions to the noted issues.

3.3.3 Proteins

Protein contour plots and accumulation graphs are provided in figure 3-5 and Figure 3-6 for 250nM BSA. Due to the reduced concentrations it is more difficult see the depletion zones developing in the contour plots but the peaks in protein concentration are still clearly visible at the interface and the same concentrating effect demonstrated with fluorescein is shown to apply to proteins as well. The asymmetry is slightly more pronounced in these cases as observed most notably in Figure 3-5A where the accumulation builds most heavily in the top right corner. While improper grounding is again partly to blame the initial concentration distribution was difficult to see due to the low concentrations resulting in low intensity images and may not have been completely uniform. There is no real increase in Figure 3-5A over the fluorescein concentration factors under similar conditions. While the simulations indicated a much higher expected outcome for slower molecules the simulations did not account for shape, adsorption and varying pH effects, factors that would need to be accounted for to accurately model protein dynamics. Figure 3-6A shows higher C^* values with a maximum of 51 at an increased source voltage of 1kV. The fact that both these protein runs occur at slower

rates (45.8s and 35.1s) than the fluorescein runs even though they are at higher field strengths is a good indication that the surface charge of the Nafion has been reduced, likely due to nonspecific protein adsorption onto its surface.

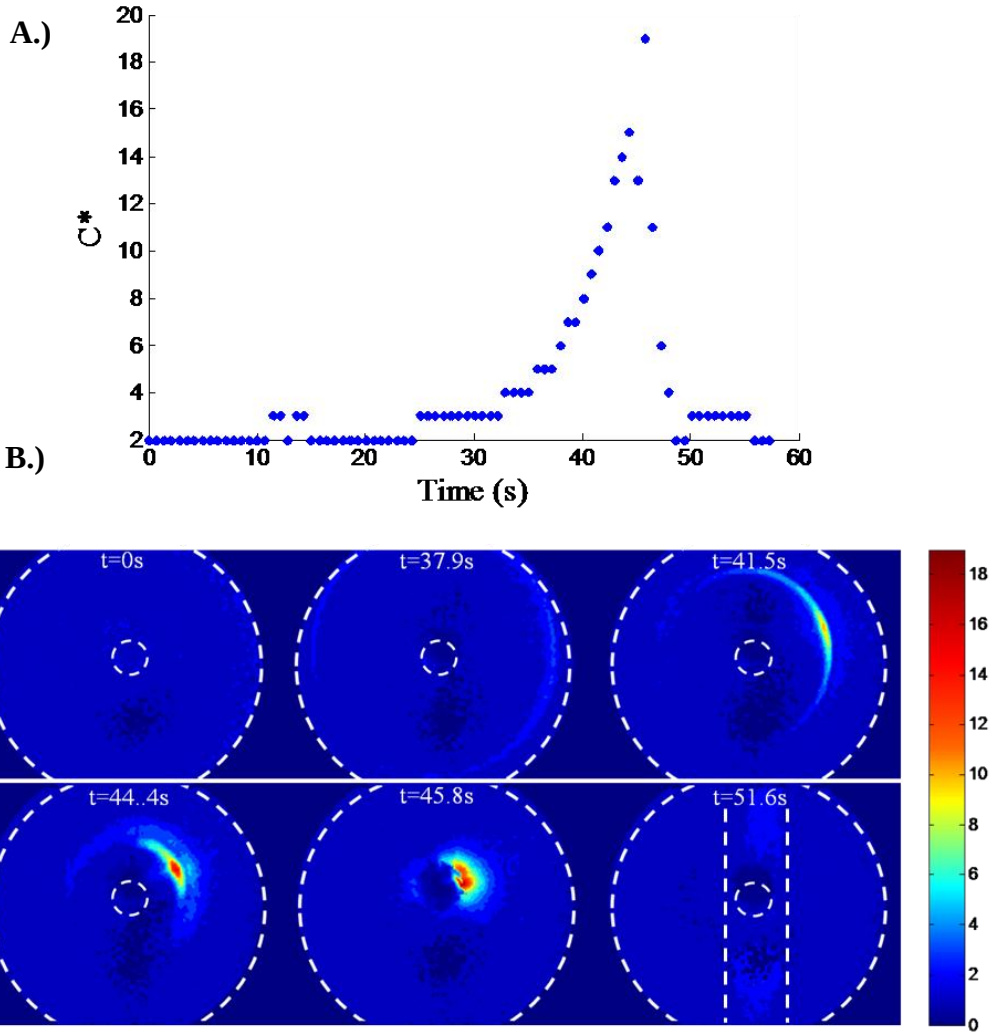

Figure 3-5| **(A)** Increase in concentration with time for 250 nM BSA with an applied voltage of 500V. **(B)** Concentration intensity plots at various stages of progression. Maximum concentration distribution is shown at t=45.8 s.

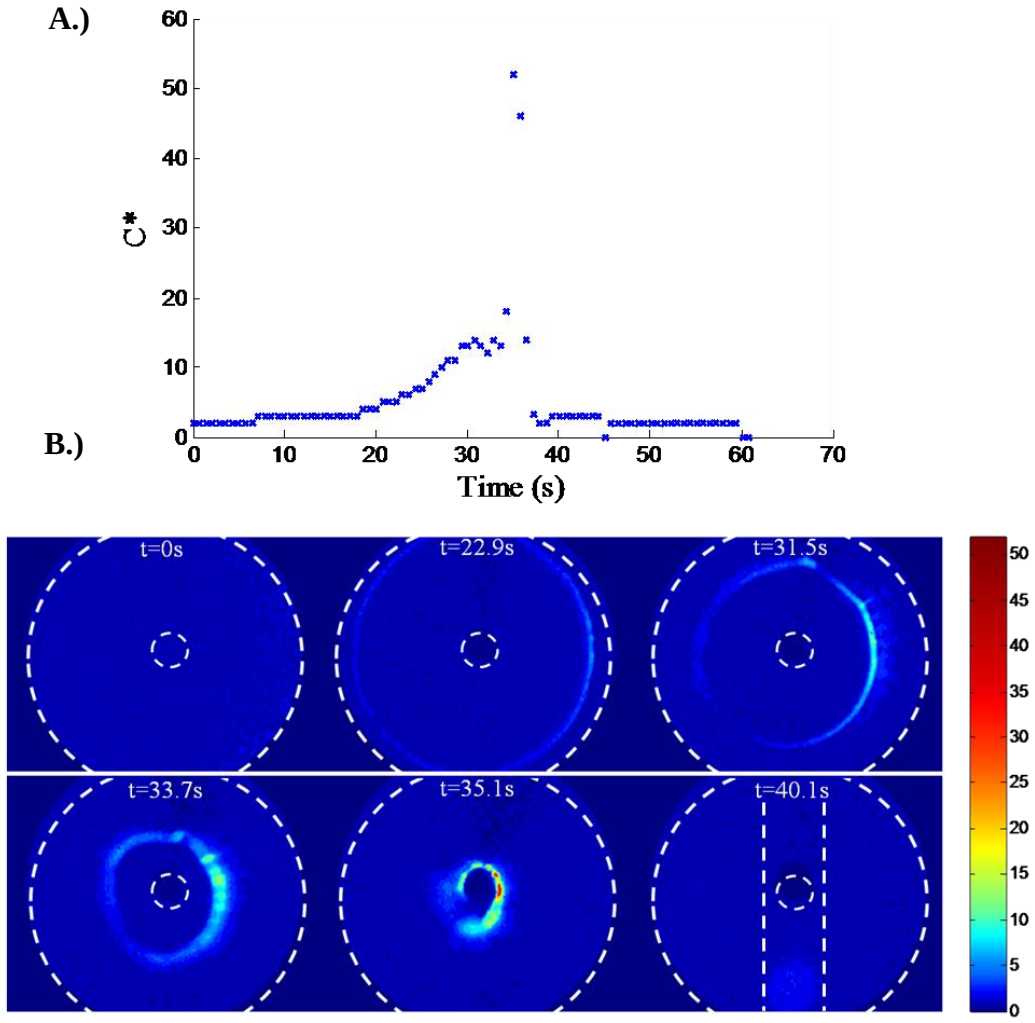

Figure 3-6| **(A)** Increase in concentration with time for 250 nM BSA with an applied voltage of 1000V. **(B)** Concentration intensity plots at various stages of progression. Maximum concentration distribution is shown at t=35.1 s.

Incorporating proteins presents a unique set of challenges as compared to the initial fluorescein trials. A protein is a sequence of amino acids each of which contains acid and base groups, it is thus a property of proteins that their surface charge varies with pH. Proteins are also macromolecules containing their own double layer and are notorious for adsorbing onto surfaces [95]. Nafion, due to its high negative surface charge has been used in sensors to prevent adsorption through static repulsion [96]. However, due to the

thin film used and the suppressed conductivity in this case the repulsive effect may be compromised. Additionally, H-form Nafion is acidic and the effectiveness of the buffer at maintaining pH = 8.1 is uncertain. As pH decreases so too does the surface charge on BSA, which is good for sample collection efficiency since mobility is reduced but could increase adsorption rates onto the Nafion. Too much non-specifically adsorbed protein on the Nafion surface could act to suppress the Nafion's effective surface charge density. A reduced surface charge density effectively slows the development of the depletion layer by reducing the number of ions within the double layer (the means by which electrical continuity is maintained in the system). The surface polarity of Nafion exhibits a large variation dependant on the hydration level so potentially by changing the Nafion pre-treatment procedure (i.e. soaking longer) the protein adsorption could be avoided [96] and results would be expected to correlate better with the large molecule simulations.

3.3.4 Equivalent Circuit Model Determination of Effective Voltage

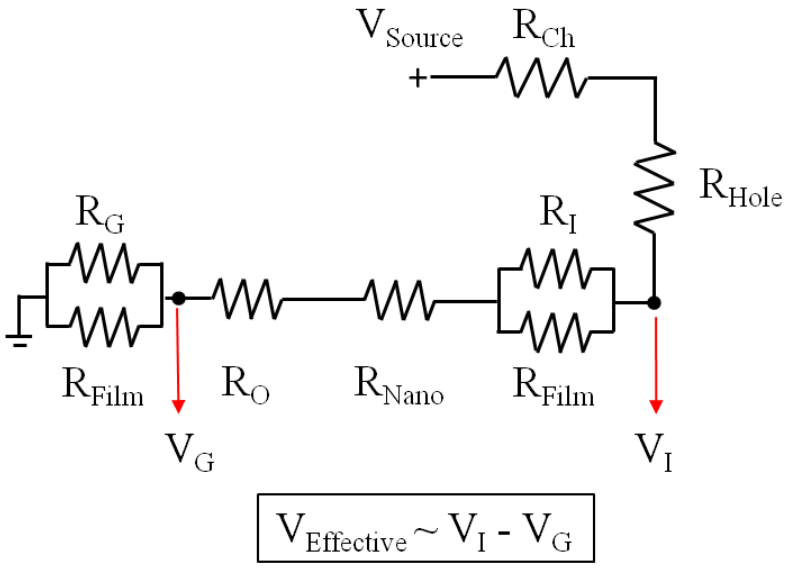

Figure 3-7| Equivalent circuit model. R_{Ch} is the upper channel resistance, R_{Hole} is the punched hole resistance, R_I is the inner chamber resistance, R_{Film} is the Nafion

film resistance, R_{Nano} is the active nano membrane resistance, R_O is the outer radial channel resistance and R_G is the resistance of the channel leading to ground.

For experimental trials the source voltage is on the order of 200-1000V, however the effective voltage difference across the preconcentration layer will vary from this applied voltage due to the various resistances within the microfluidic network. To estimate the effective voltage an equivalent wiring diagram was used (Figure 3-7) where resistances are calculated in a similar manner to [97] using the relationship

$$R_i = \frac{1}{\kappa} \times \frac{L_i}{A_i} \tag{3.2}$$

Where R_i is the resistance, κ, L_i and A_i are the conductivity, path length and cross sectional area respectively. The conductivity of the BGE was measured using a conductivity meter as $488\ \mu S/cm$. The currents within the inner radial chamber and the grounding channel have two paths through which to travel, the bulk solution or the Nafion film. The resistance here is calculated as an equivalent resistance of two resistors in parallel. The same equivalence is not performed for the outer radial channel since this is on the enrichment side of the membrane and thus the solution will see an increase in conductivity and should dominate as the preferential current path. The voltage difference across the microfluidic network can be calculated using a voltage divider formula

$$V_I = \frac{R_{equiv,I} + R_{Nano} + R_O + R_{equiv,G}}{\sum R_i} \times V_{Source} \tag{3.3}$$

And likewise for V_G

$$V_G = \frac{R_{equiv,G}}{\sum R_i} \times V_{Source} \tag{3.4}$$

As the depletion region develops within the radial chamber one would expect V_I to increase as the conductivity within the solution drops. Through modeling simulations the conductivity was estimated to decrease by a factor of 200 within the depletion region. The effective voltage, $V_{Effective}$, was calculated for the initial experimental condition where the radial chamber is filled with buffer (high conductivity) solution and the end condition where the radial chamber is filled with the depleted buffer (low conductivity) solution. The conductivity of Nafion is known to be suppressed in recast films [71] so κ_{Nafion} was used as a fitting parameter within the model with the value being determined as $\kappa_{Nafion} = 0.00145\ S/cm$. Such a value is in line with results reported within Ref. [71] for nanometer thick films at room temperature. With given values and a source voltage of 400V the voltage varied little between the non-depleted (~94 V) and depleted (~95 V) times. An accurate fit to experimental data could thus be gained by applying a constant voltage boundary condition $V_{Effective}$ taken as 95V. Calculation and parameter details are available in Appendix B.

3.4 Summary

The use of radial geometries was presented in this chapter showing several distinct benefits over established axial methods. Using radial configurations provides the following benefits 1) the non-linear interfacial effects confine and focus samples to small central regions 2) ease of coupling with integrated microsystems since larger initial volumes are focused and can be injected into secondary analysis layers 3) the process is multidimensional leading to an increased interfacial area and increased ionic currents 4) fabrication uses standard soft lithographic methods with the only additional step required being the spin coating of a Nafion membrane 5) simple micro-scale fabrication may be

used to define the effective geometry of the nanoporous membrane 6) patterning and bonding of intermediate membrane layers is avoided since the entire bottom substrate of the chip assembly is coated with the membrane.

Radial concentration of Fluorescein and FITC-BSA protein were both successfully demonstrated for the first time in this format with a maximum increase in FITC-BSA of $50\times$ accomplished within 35.1 s. The 1-D radial numerical model showed good agreement with the fluorescein experimental data lending credibility to the projections made in Chapter 2. While the promise of the technique is clear some issues were encountered regarding the stability of the depletion interface at increased voltages and high BGE conductivities, issues that are further investigated in the next chapter.

Chapter 4. Alternative Microstructure Geometries with Planar Nanoporous Films

4.1 Introduction

The use of planar nanoporous films provides the unique advantage that membranes do not have to be patterned; rather the microchannels define the active membrane/channel interface. Creating alternative layouts becomes a simple matter of designing and fabricating the microfluidic chip. In this chapter several variations in geometry are demonstrated for explorative purposes and to resolve electrokinetic instability issues that arose in previous efforts at high voltages and high BGE conductivities. There have been several studies of note done on electrokinetic instabilities in the presence of varying conductivities showing that instabilities arise due to the mismatch of fields and velocities at large conductivity gradients [81-83]. They have found stability generally depends on an electric Rayleigh number and conductivity ratio defined as

$$Ra(1-\gamma) = \frac{\epsilon_0 \epsilon_r E_0^2 H}{D\mu} \cdot \left(\frac{\sigma_{High} - \sigma_{Low}}{\sigma_{Low}}\right) \tag{4.1}$$

Where H is the channel height, D is diffusivity as before, E_0 is the applied electric field and σ_{High} and σ_{Low} are the conductivities in the high and low regions. While the stability criteria developed within those studies is not directly applicable here due to the unique geometries and high surface charge densities encountered it has been experimentally observed that equation (4.1) contains most of the relevant parameters that determine the stability of the system. Namely, as $Ra(1-\gamma)$ increases, the likelihood of instability arising increases, other factors that are observed to have effect are geometrical in nature. While channel height is seen to effect stability, the relative confinement of the solution in

lateral directions has an effect as well. Notably, as the focusing chamber radius decreases so too does the influence of instability. Intuitively this dependency makes sense, as the fluid becomes more confined viscous forces have more affect and serve to dampen any instabilities.

4.2 Fully Planar Configuration

The most easily fabricated microstructures are those that are fully planar. While the radial preconcentration layers detailed in Chapter 3 were fully planar they required a top channel in which to inject the sample. This requires alignment and filling of multilevel structures which can be difficult (air bubbles often become trapped in the vertically punched hole connecting the two layer necessitating vacuum assisted filling [94]). To facilitate a fully planar structure a semi-circular focusing chamber is used with an exit channel leading to the anode. Figure 4-1 illustrates the layout and function of the device.

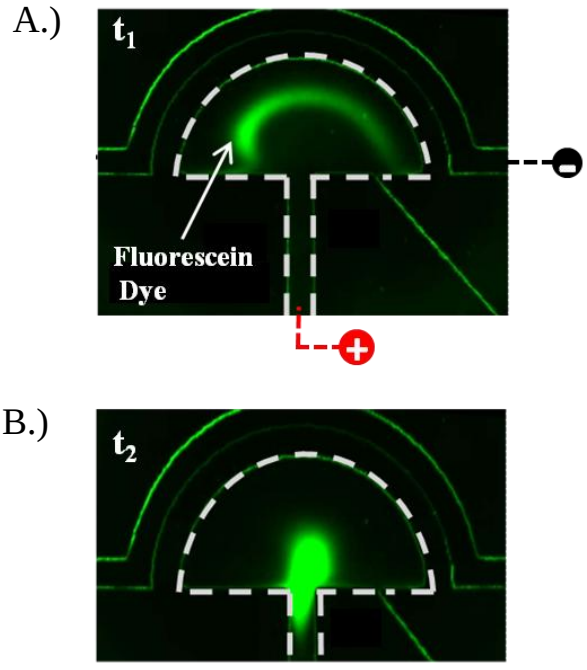

Figure 4-1| Illustration of semi-circular layout (Fluorescent Images). **(A)** The focusing chamber is connected to the anode compartment via a planar channel. An outer

channel is grounded applying a potential difference across the intermediate membrane region. At some time t_1 the depletion region starts to focus the sample. **(B)** At some later time t_2 the sample is focused at the outlet channel entrance prior to being forced down the channel.

The progressing depletion zone is seen in the intensity plots of Figure 4-2A while the time evolution of peak C^* is plotted in Figure 4-2B. The characteristic radial focusing is still observed in this instance with a qualitatively similar non-linear peak concentration profile (Figure 4-2B) as demonstrated in the numerical simulations. Only a marginal increase in concentration of $2.5\times$ is seen for this layout at an applied voltage of 50V. While being the easiest geometry to fabricate the concentration efficiency was largely compromised by having a relatively large outlet channel ($width = 200\mu m$) on the same plane since much of the sample was drawn down the channel prior to the depletion zone corralling it.

A.)

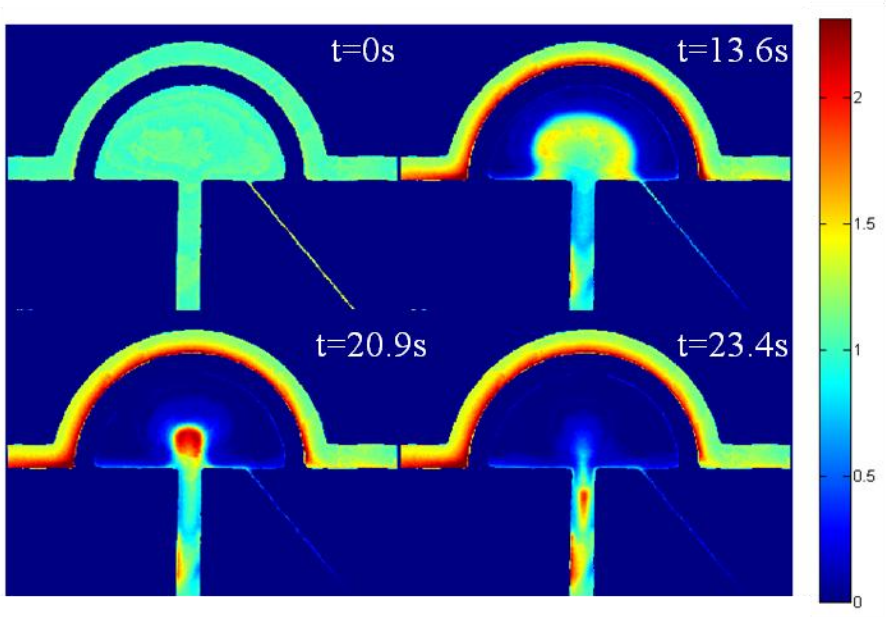

B.)

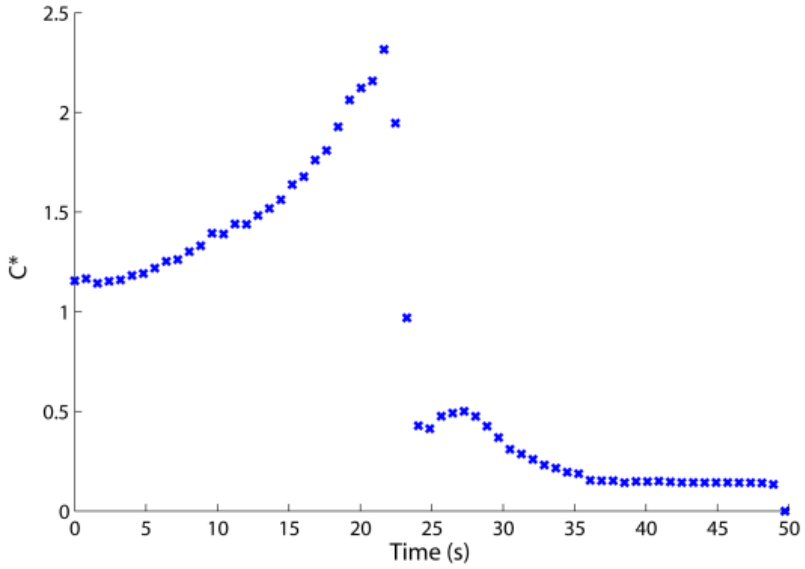

Figure 4-2| Half radial fully planar geometry at 50 V source voltage with chamber diameter = 1.44 mm and $h_{ch} = 100\ \mu m$. The solution is 100 μM fluorescein in1X TAE buffer. **(A)** Intensity plots of the fluorescein concentration at various stages of progression. The lower right channel visible at t = 0 s is an outlet port to assist filling. **(B)** Peak C* evolution with time.

The method demonstrates fully planar configurations would work though modifications to the present design would be necessary. Potentially narrowing or tapering the anode channel could help to reduce analyte 'leakage' flux.

4.2.1 Multiplexed Planar Configuration

Use of a uniform planar nanoporous film as the substrate allows extension of the concept to far more complicated microchannel geometries. The same semi-circular planar geometry established in the previous section is maintained however a multiplexed approach is implemented here. Figure 4-3A illustrates the layout of the multiplexed design which has 4 radial chambers capable of injecting concentrated plugs sequentially into a common channel. The visible window is indicated by the green dotted rectangle and the resultant time evolution of peak C^* is shown in Figure 4-3B for the 3 visible channels at an applied voltage of 400V. A contrast enhanced fluorescence image sequence is shown in Figure 4-3C.

A.)

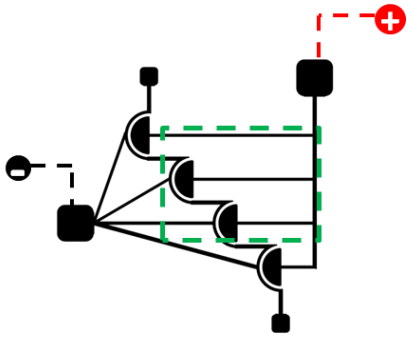

B.)

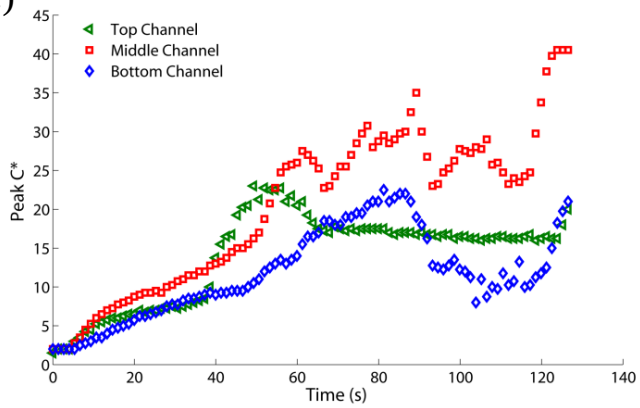

C.)

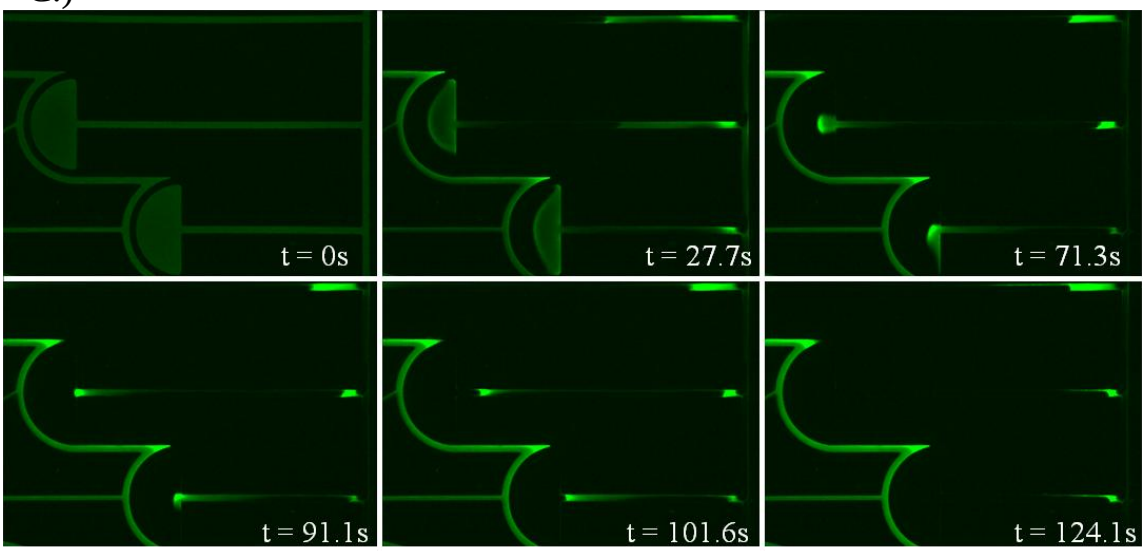

Figure 4-3| **(A)** Layout of the multiplexed design with the microscope visible area indicated by the green dotted rectangle. **(B)** Time evolution of peak $\boldsymbol{C}^*$ for the three visible channels. The middle channel attains the highest $\boldsymbol{C}^*$ value at ~40. **(C)** (Contrast Enhanced) Image sequence showing the concentration effect and the concentrated plugs travelling down the connecting channels.

The concentration effect is demonstrated in all three visible channels though to varying degrees. One of the main causes of the nonuniform concentration effect between channels is the grounding. The grounding channels did not satisfactorily provide a uniform potential across the active membrane area resulting in asymmetric depletion evolution and varying concentration enhancement from channel to channel. The other main issue encountered was the concentrated plugs did not inject into the common channel. Instead it was found that the samples collected at the channel branches. This is an interesting effect and is worthy of further investigation. It is noteworthy that such effects arising from multiplexed concentrating elements are unique to this work.

While process refinement and characterization is required the promise of multiplexing using the presented method is clearly evident, as are opportunities for simultaneous concentration and control of multiple samples using this method.

4.3 Electrokinetic Instabilites

Through the many experiments performed in this thesis work, it was found that electrokinetic instabilities (EKI) mentioned in the introduction to this chapter can induce mixing, destroy the focusing effect, and lead to uncertainties. One such case demonstrating EKI is seen in Figure 4-4 where a large diameter focusing chamber (d = 7 mm) was used with four support posts. At an applied voltage of 160 V the evolution of the depletion zone quickly deviates from the uniform radial progression previously observed and degrades into a chaotic form. The fingering pattern is common where high peak concentrations can be seen trapped within the 'finger tips' but the peaks are highly transient being destroyed by the instabilities on a timescale of seconds. The height of the microfluidic channels in this instance are $100\mu m$, an increase over the radial chips of Chapter 3 which were only $20\mu m$. The use of the $20\mu m$ channel heights was found to aid significantly in avoiding instabilities.

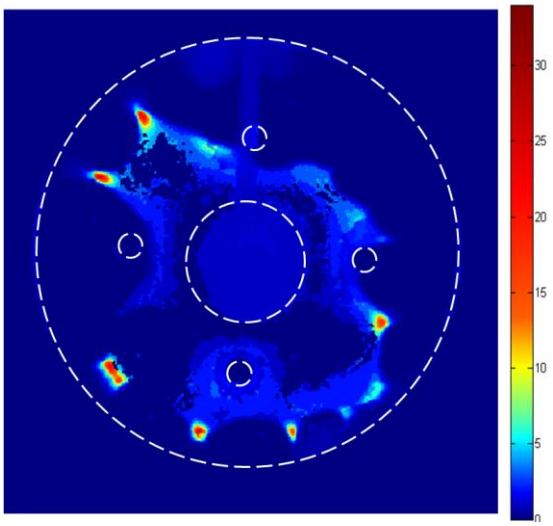

Figure 4-4| Instability at 160 V with focusing chamber (w/posts) diameter =7 mm, $h_{ch} = 100\ \mu m$. 1X TAE buffer and 100 μM fluorescein tracer

4.4 Finned Geometries for Reducing EKI

Noting that a reduced channel height aids in preventing the onset of instabilities the next design step was to explore further confinement of the fluid through structures within the radial focusing chamber. Radial fins were introduced in a larger focusing chamber (d= 7mm) with a height of $40\mu m$. A larger height is allowable in this instance due to the introduction of the fins which serve to laterally confine the fluid. The fluorescence images for an applied voltage of 200V are seen in Figure 4-5A. With the introduction of the fins a uniform radial depletion region develops gathering and focusing the sample before injecting it into the upper channel. The slightly oval shape of the concentrated region, as visible in the third frame of Figure 4-4A (t = 28.8s) is due to the position of the grounding channels (on left and right - not shown). The effect is small, due in large part to the electric field control provided by the finned design, and quickly rectified as indicated by the circular concentrated region in the fourth frame (t = 37.1 s). Importantly, this result indicates that the finned chamber geometry effectively reduces the EKI

influence and results in a uniform radial concentration effect. As compared to a fully open chamber, the fins require 40% of the area. This increased area, for a similar focusing volume is a small price to pay for repeatable, instability-free performance.

Of note here is the reduced dispersion of the injected plug, looking at Figure 4-5B it's seen that the concentrated plug loses little of its concentration increase while traveling through the channel. This can be explained recalling the expression for area averaged velocity within the microchannel from Chapter 2 (Table 3). Solving for the pressure term

$$-\frac{dP}{dr} = \frac{12\mu}{h^3}(Q_{ch} - hU_{EO}) \tag{4.2}$$

Where Q_{ch} is the flow rate in the microchannel and U_{EO} is the electroosmotic velocity. The flow rate through the membrane is the rate determining factor so assuming Q_{ch} does not vary with an increase in channel height it's seen that a reduction in the induced pressure gradient must occur to satisfy continuity. Since pressure scales to the third power of the microchannel height the effective pressure is dramatically reduced resulting in the reduced dispersion of the ejected plug.

A.)

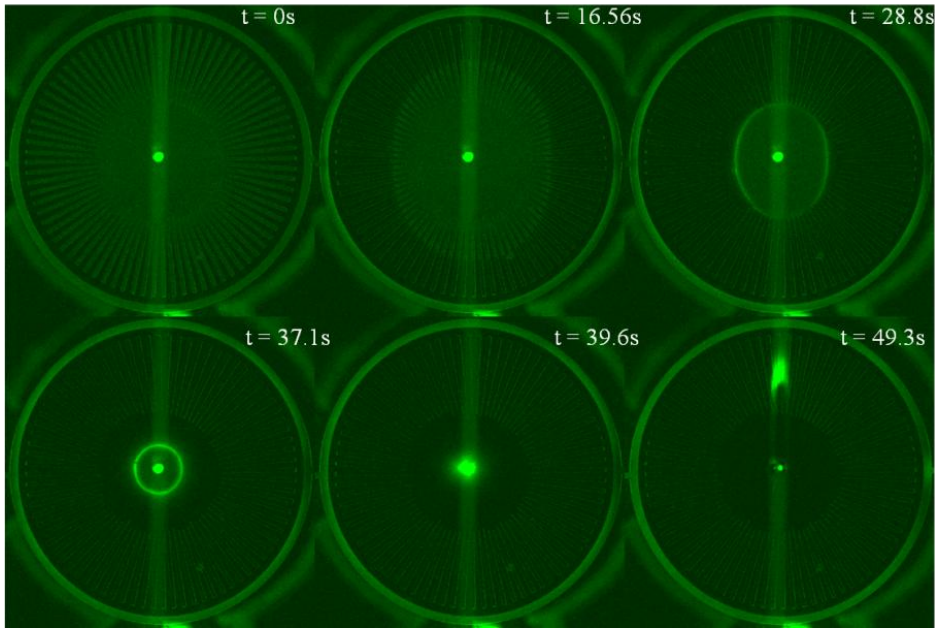

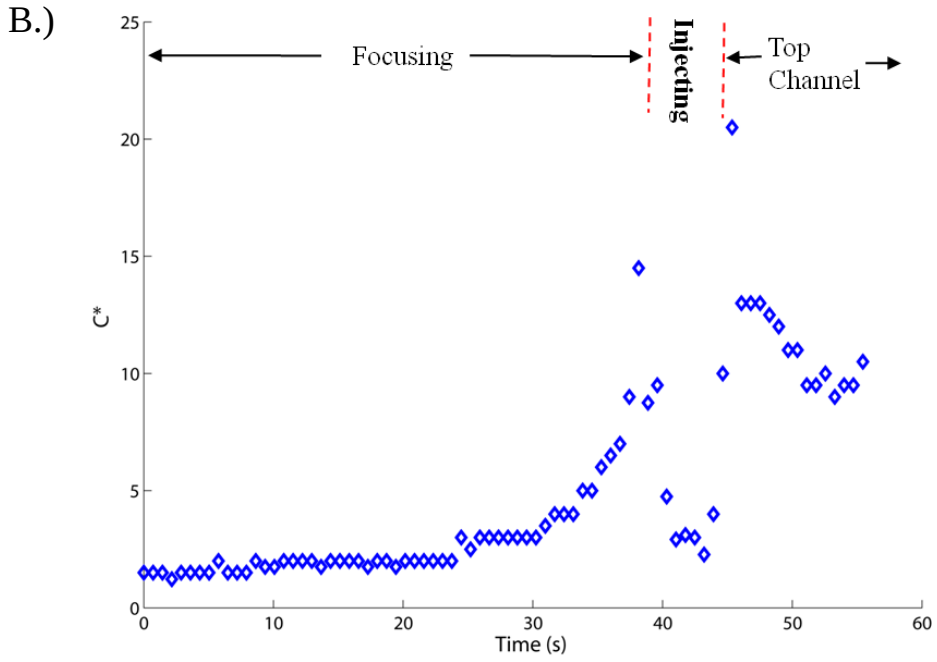

Figure 4-5| Radial finned geometry. **(A)** Contrast enhanced fluorescent image sequence of radial finned geometry. The applied voltage is 200 V with a 5 μM fluorescein solution in 10 mM TAE buffer. Channel height = 40 μm, fin width = 170 μm spaced 100 μm apart and chamber diameter = 7mm. **(B)** Time evolution of peak C^*. The maximum value reaches 20 once the plug is injected into the top channel.

4.5 Summary

The application of a planar nanoporous film to various microchannel geometries was demonstrated, namely planar and multiplexed planar methods were shown to be possible. A semi-circular geometry demonstrated the feasibility of the fully planar approach. This led to a scaled up multiplexed method using multiple focusing channels in parallel. Samples were observed to collect in the channel branches, a unique and unexpected effect. While the method suffered from grounding issues it served as proof-of-concept and warrants further investigation.

To optimize the radial method high field strengths and high BGE mobilities are required, however the increase in these parameters contributes to the onset of EKI, the destructive effects of which were shown. To help mitigate the effect fins were introduced into the radial design to better confine the fluid, the resultant uniform radial concentration profile was a good indication that the finned chamber geometry effectively reduces the EKI influence. The improved lateral confinement afforded by the fins allowed for an increased channel height that produced less dispersive sample plugs once ejected into the top channel.

Chapter 5. Conclusions and Future Work

This thesis investigated an analyte concentration strategy based on a single microfluidic layer on a uniform nanoporous film. A combination of numerical and experimental techniques were employed to determine the effectiveness of such a method. The contributions of this work included development of a radial concentration polarization model with a highly charged uniform nanoporous film that was used to extend experimental works. Experimental work included the fabrication of radial micro-structures on a Nafion film allowing the first ever demonstration of radial CP used to concentrate and focus fluorescein and protein molecules. Further proof of concept designs were also demonstrated including finned geometries to reduce EKI effects and multiplexed layouts demonstrating simultaneous manipulation of multiple samples.

5.1 Radial Concentration Polarization with Nanoporous Membranes

A continuum based numerical model was developed to model concentration polarization in a microchannel at the interface of a highly charged nanoporous domain. Concentration and potential distributions along with velocity profiles were determined for a nanopore and scaled up to provide properties within a thin nanoporous membrane region. It was seen that the propagation of the depletion zone was an unsteady process that could be used to corral slower analyte molecules at the depletion interface producing a concentration enrichment effect. Factors such as the electric field strength, BGE ion mobilities and analyte ion mobility were shown to have a strong effect on the concentration enhancement. Importantly, these results demonstrated operation of a radial analyte concentration scheme. This is the first work in this area as all other concentration

schemes have been 1-D axial within a channel with low surface charge densities. The model is capable of reproducing the non-linear peak concentration time evolution characteristics observed experimentally.

5.2 Experimental Concentration of Molecules with Radial Micro-Structures

The use of radial geometries was presented showing several distinct benefits over established axial methods, the following advantages were noted:

1) The use of radial geometries allows the non-linear interfacial effects to confine and focus samples to small central regions
2) The layout is amenable to coupling with integrated microsystems since larger initial volumes are focused and can be injected into secondary analysis layers
3) The multidimensional process leads to an increased interfacial area and increased ionic currents
4) No flow balancing via pressure driven flows is required and no optimum ratio of tangential and normal electric fields need be obtained, as compared to previous concentration schemes [56-61]
5) Fabrication procedures are planar and use standard soft lithography with the only additional step required being the spin coating of a Nafion membrane, that is, simple microfluidic-scale fabrication may be used to define the effective geometry of the nanofluidics
6) The entire bottom substrate of the chip assembly is coated with the membrane removing issues associated with patterning and bonding of intermediate layers

Radial concentration of Fluorescein and FITC-BSA protein were both successfully demonstrated experimentally for the first time in this format with a maximum increase in FITC-BSA of 50 × accomplished within 35.1 s.

5.3 Demonstration of Alternative Geometries

The application of a planar nanoporous film to various microchannel geometries was demonstrated, namely planar and multiplexed planar methods were shown to be possible. A semi-circular geometry demonstrated the feasibility of the fully planar approach. This led to a scaled up proof-of-concept multiplexed method using multiple focusing channels in parallel. Samples were observed to collect in the channel branches, a unique and unexpected effect.

To help mitigate the destructive effects of EKI fin structures were introduced into the radial design to better confine the fluid, the resultant uniform radial concentration profile was a good indication that the finned chamber geometry effectively reduced the EKI influence. The improved lateral confinement afforded by the fins allowed for an increased channel height that produced less dispersive sample plugs once ejected into the top channel.

5.4 Proposed Future Work

Some aspects of this work could be extended for study in future projects, some suggested areas are listed:

1) Devising a more uniform and effective grounding strategy. Presently the grounding channels are not at a uniform potential which gives rise to asymmetries in the radial

focusing. Potentially adding additional grounding channels or devising other means to ground the outer channels would benefit the work.

2) Determining the effect of Nafion pre-treatment on protein concentration rates. It is thought that hydrating the Nafion substrate for long durations in the buffer solution prior to chip assembly would ensure the Nafion structure has a negative surface thus repulsing negatively charged proteins and limiting non-specific adsorption, though further study is required.
3) Implementing improved voltage switching schemes for the purpose of improving plug injection. Namely, investigating removal of the grounding electrodes once the sample plug has been focused to see if this aids in the reduction of dispersive pressure driven flows.
4) Studying the finned geometries at higher voltages to verify EKI effects are still limited and looking at the effect of fin spacing. Alternative geometries incorporating thinner fins could be examined and the optimum fin volume to chamber volume ratio could be determined.
5) Further experiments with multiplexed geometries could be performed. This would help to determine the cause of the samples collecting in the branches and refine the channel design so that sequential injection of concentrated plugs into a connecting channel could be performed.
6) Given the flexibility the planar nanoporous membrane affords in terms of channel architectures further study on new and unique geometries could be explored.

Bibliography

[1] A. Manz, *et al.*, "DESIGN OF AN OPEN-TUBULAR COLUMN LIQUID CHROMATOGRAPH USING SILICON CHIP TECHNOLOGY," 1990, pp. 249-255.

[2] G. M. Whitesides, "The origins and the future of microfluidics," *Nature*, vol. 442, pp. 368-373, Jul 2006.

[3] G. M. Whitesides and A. D. Stroock, "Flexible methods for microfluidics," *Physics Today*, vol. 54, pp. 42-48, Jun 2001.

[4] D. J. Beebe, *et al.*, "Physics and applications of microfluidics in biology," *Annual Review of Biomedical Engineering*, vol. 4, pp. 261-286, 2002.

[5] C. D. Chin, *et al.*, "Lab-on-a-chip devices for global health: Past studies and future opportunities," *Lab on a Chip*, vol. 7, pp. 41-57, 2007.

[6] P. Yager, *et al.*, "Microfluidic diagnostic technologies for global public health," *Nature*, vol. 442, pp. 412-418, 2006.

[7] V. Linder, "Microfluidics at the crossroad with point-of-care diagnostics," *Analyst*, vol. 132, pp. 1186-1192, 2007.

[8] A. W. Martinez, *et al.*, "Simple telemedicine for developing regions: Camera phones and paper-based microfluidic devices for real-time, off-site diagnosis," *Analytical Chemistry*, vol. 80, pp. 3699-3707, 2008.

[9] J. M. Ramsey, *et al.*, "MICROFABRICATED CHEMICAL MEASUREMENT SYSTEMS," *Nature Medicine*, vol. 1, pp. 1093-1096, Oct 1995.

[10] T. M. Squires and S. R. Quake, "Microfluidics: Fluid physics at the nanoliter scale," *Reviews of Modern Physics*, vol. 77, pp. 977-1026, Jul 2005.

[11] J. P. Brody, *et al.*, "Biotechnology at low Reynolds numbers," *Biophysical Journal*, vol. 71, pp. 3430-3441, 1996.

[12] G. B. West, *et al.*, "The fourth dimension of life: Fractal geometry and allometric scaling of organisms," *Science,* vol. 284, pp. 1677-1679, 1999.

[13] A. Manz and J. C. T. Eijkel, "Miniaturization and chip technology. What can we expect?," *Pure and Applied Chemistry,* vol. 73, pp. 1555-1561, 2001.

[14] H. A. Stone, *et al.*, "Engineering flows in small devices: Microfluidics toward a lab-on-a-chip," *Annual Review of Fluid Mechanics,* vol. 36, pp. 381-411, 2004.

[15] A. J. Tudos, *et al.*, "Trends in miniaturized total analysis systems for point-of-care testing in clinical chemistry," *Lab on a Chip,* vol. 1, pp. 83-95, 2001.

[16] M. G. Pollack, *et al.*, "Electrowetting-based actuation of droplets for integrated microfluidics," *Lab on a Chip,* vol. 2, pp. 96-101, 2002.

[17] J. Atencia and D. J. Beebe, "Controlled microfluidic interfaces," *Nature,* vol. 437, pp. 648-655, 2005.

[18] B. Zhao, *et al.*, "Surface-directed liquid flow inside microchannels," *Science,* vol. 291, pp. 1023-1026, 2001.

[19] L. Shui, *et al.*, "Multiphase flow in lab on chip devices: A real tool for the future," *Lab on a Chip,* vol. 8, pp. 1010-1014, 2008.

[20] M. K. Chaudhury and G. M. Whitesides, "HOW TO MAKE WATER RUN UPHILL," *Science,* vol. 256, pp. 1539-1541, 1992.

[21] S. Pennathur, *et al.*, "How to exploit the features of microfluidics technology," *Lab on a Chip,* vol. 8, pp. 20-22, 2008.

[22] D. Erickson, *et al.*, "A miniaturized high-voltage integrated power supply for portable microfluidic applications," *Lab on a Chip,* vol. 4, pp. 87-90, 2004.

[23] S. Pennathur, "Flow control in microfluidics: are the workhorse flows adequate?," *Lab on a Chip,* vol. 8, pp. 383-387, 2008.

[24] R. F. Probstein, *Physiochemical Hydrodyanmics: An Introduction,* Second ed. New Jersey: Wiley-Interscience, 1994.

[25] R. B. Schoch, *et al.*, "Transport phenomena in nanofluidics," *Reviews of Modern Physics,* vol. 80, pp. 839-883, Jul-Sep 2008.

[26] J. Newman and K. E. Thomas-Alyea, *Electrochemical Systems*, 3 ed.: John Wiley & Sons, 2004.

[27] R. J. Hunter, *Zeta Potential in Colloid Science*. London: Academic Press.

[28] T. Thorsen, *et al.*, "Microfluidic large-scale integration," *Science,* vol. 298, pp. 580-584, 2002.

[29] D. Juncker, *et al.*, "Autonomous microfluidic capillary system," *Analytical Chemistry,* vol. 74, pp. 6139-6144, 2002.

[30] J. C. T. Eijkel and A. van den Berg, "Young 4ever - the use of capillarity for passive flow handling in lab on a chip devices," *Lab on a Chip,* vol. 6, pp. 1405-1408, 2006.

[31] R. S. Foote, *et al.*, "Preconcentration of proteins on microfluidic devices using porous silica membranes," *Analytical Chemistry,* vol. 77, pp. 57-63, Jan 2005.

[32] J. C. T. Eijkel and A. van den Berg, "Nanofluidics: what is it and what can we expect from it?," *Microfluidics and Nanofluidics,* vol. 1, pp. 249-267, Jul 2005.

[33] R. Karnik, *et al.*, "Electrostatic control of ions and molecules in nanofluidic transistors," *Nano Letters,* vol. 5, pp. 943-948, May 2005.

[34] J. Y. Han, *et al.*, "Molecular sieving using nanofilters: Past, present and future," *Lab on a Chip,* vol. 8, pp. 23-33, 2008.

[35] H. Daiguji, *et al.*, "Ion transport in nanofluidic channels," *Nano Letters,* vol. 4, pp. 137-142, Jan 2004.

[36] Q. S. Pu, *et al.*, "Ion-enrichment and ion-depletion effect of nanochannel structures," *Nano Letters,* vol. 4, pp. 1099-1103, Jun 2004.

[37] A. Plecis, *et al.*, "Ionic transport phenomena in nanofluidics: Experimental and theoretical study of the exclusion-enrichment effect on a chip," *Nano Letters,* vol. 5, pp. 1147-1155, Jun 2005.

[38] M. Nishizawa, *et al.*, "METAL NANOTUBULE MEMBRANES WITH ELECTROCHEMICALLY SWITCHABLE ION-TRANSPORT SELECTIVITY," *Science,* vol. 268, pp. 700-702, May 1995.

[39] W. M. Deen, "HINDERED TRANSPORT OF LARGE MOLECULES IN LIQUID-FILLED PORES," *Aiche Journal,* vol. 33, pp. 1409-1425, Sep 1987.

[40] D. Burgreen and F. R. Nakache, "ELECTROKINETIC FLOW IN ULTRAFINE CAPILLARY SLITS," *Journal of Physical Chemistry,* vol. 68, pp. 1084-&, 1964.

[41] C. L. Rice and Whitehea.R, "ELECTROKINETIC FLOW IN A NARROW CYLINDRICAL CAPILLARY," *Journal of Physical Chemistry,* vol. 69, pp. 4017-&, 1965.

[42] S. Levine, *et al.*, "THEORY OF ELECTROKINETIC FLOW IN FINE CYLINDRICAL CAPILLARIES AT HIGH ZETA-POTENTIALS," *Journal of Colloid and Interface Science,* vol. 52, pp. 136-149, 1975.

[43] R. J. Gross and J. F. Osterle, "MEMBRANE TRANSPORT CHARACTERISTIC OF ULTRAFINE CAPILLARIES," *Journal of Chemical Physics,* vol. 49, pp. 228-&, 1968.

[44] E. H. Cwirko and R. G. Carbonell, "TRANSPORT OF ELECTROLYTES IN CHARGED PORES - ANALYSIS USING THE METHOD OF SPATIAL AVERAGING," *Journal of Colloid and Interface Science,* vol. 129, pp. 513-531, May 1989.

[45] S. Pennathur and J. G. Santiago, "Electrokinetic transport in nanochannels. 1. Theory," *Analytical Chemistry,* vol. 77, pp. 6772-6781, Nov 2005.

[46] A. De Leebeeck and D. Sinton, "Ionic dispersion in nanofluidics," *Electrophoresis,* vol. 27, pp. 4999-5008, Dec 2006.

[47] A. Holtzel and U. Tallarek, "Ionic conductance of nanopores in microscale analysis systems: Where microfluldics meets nanofluidics," *Journal of Separation Science,* vol. 30, pp. 1398-1419, Jul 2007.

[48] R. S. Eisenberg, "From structure to function in open ionic channels," *Journal of Membrane Biology,* vol. 171, pp. 1-24, Sep 1999.

[49] T. C. Kuo, *et al.*, "Gateable nanofluidic interconnects for multilayered microfluidic separation systems," *Analytical Chemistry,* vol. 75, pp. 1861-1867, Apr 2003.

[50] R. Karnik, *et al.*, "Field-effect control of protein transport in a nanofluidic transistor circuit," *Applied Physics Letters,* vol. 88, p. 3, Mar 2006.

[51] J. A. Manzanares, *et al.*, "NUMERICAL-SIMULATION OF THE NONEQUILIBRIUM DIFFUSE DOUBLE-LAYER IN ION-EXCHANGE MEMBRANES," *Journal of Physical Chemistry,* vol. 97, pp. 8524-8530, Aug 1993.

[52] R. F. Probstein, *Physiochemical Hydrodyanmics: An Introduction,* Second ed. New Jersey: Wiley-Interscience.

[53] A. Mani, *et al.*, "On the Propagation of Concentration Polarization from Microchannel-Nanochannel Interfaces Part I: Analytical Model and Characteristic Analysis," *Langmuir,* vol. 25, pp. 3898-3908, Mar 2009.

[54] A. Plecis, *et al.*, "Electropreconcentration with Charge-Selective Nanochannels," *Analytical Chemistry,* vol. 80, pp. 9542-9550, Dec 2008.

[55] F. G. Donnan, "THEORY OF MEMBRANE EQUILIBRIA AND MEMBRANE-POTENTIALS IN THE PRESENCE OF NON-DIALYZING ELECTROLYTES - A CONTRIBUTION TO PHYSICAL-CHEMICAL PHYSIOLOGY (REPRINTED FROM ZEITSHRIFT FUR ELEKTROCHEMIE UND ANGEWANDTE PHYSIKALISCHE CHEMIE, VOL 17, PG 572, 1911)," *Journal of Membrane Science,* vol. 100, pp. 45-55, Mar 1995.

[56] S. J. Kim and J. Y. Han, "Self-sealed vertical polymeric nanoporous-junctions for high-throughput nanofluidic applications," *Analytical Chemistry,* vol. 80, pp. 3507-3511, May 2008.

[57] J. H. Lee, *et al.*, "Poly(dimethylsiloxane)-based protein preconcentration using a nanogap generated by junction gap breakdown," *Analytical Chemistry,* vol. 79, pp. 6868-6873, Sep 2007.

[58] J. H. Lee, *et al.*, "Increase of reaction rate and sensitivity of low-abundance enzyme assay using micro/nanofluidic preconcentration chip," *Analytical Chemistry,* vol. 80, pp. 3198-3204, May 2008.

[59] J. H. Lee, *et al.*, "Multiplexed proteomic sample preconcentration device using surface-patterned ion-selective membrane," *Lab on a Chip,* vol. 8, pp. 596-601, 2008.

[60] Y. C. Wang, *et al.*, "Million-fold preconcentration of proteins and peptides by nanofluidic filter," *Analytical Chemistry,* vol. 77, pp. 4293-4299, Jul 2005.

[61] D. P. Wu and A. J. Steckl, "High speed nanofluidic protein accumulator," *Lab on a Chip,* vol. 9, pp. 1890-1896, 2009.

[62] R. Qiao and N. R. Aluru, "Ion concentrations and velocity profiles in nanochannel electroosmotic flows," *Journal of Chemical Physics,* vol. 118, pp. 4692-4701, 2003.

[63] M. W. Verbrugge and R. F. Hill, "ANALYSIS OF PROMISING PERFLUOROSULFONIC ACID MEMBRANES FOR FUEL-CELL ELECTROLYTES," *Journal of the Electrochemical Society,* vol. 137, pp. 3770-3777, Dec 1990.

[64] Y. Yang and P. N. Pintauro, "Multicomponent space-charge transport model for ion-exchange membranes with variable pore properties," *Industrial & Engineering Chemistry Research,* vol. 43, pp. 2957-2965, Jun 2004.

[65] T. Colinart, *et al.*, "Transport in PFSA membranes," *Journal of the Electrochemical Society,* vol. 155, pp. B244-B257, 2008.

[66] D. Hlushkou, *et al.*, "The influence of membrane ion-permselectivity on electrokinetic concentration enrichment in membrane-based preconcentration units," *Lab on a Chip,* vol. 8, pp. 1153-1162, 2008.

[67] X. Z. Jin, *et al.*, "Induced electrokinetic transport in micro-nanofluidic interconnect devices," *Langmuir,* vol. 23, pp. 13209-13222, Dec 2007.

[68] F. Baldessari, "Electrokinetics in nanochannels - Part I. Electric double layer overlap and channel-to-well equilibrium," *Journal of Colloid and Interface Science,* vol. 325, pp. 526-538, Sep 2008.

[69] B. T. Hughes, *et al.*, "One-dimensional axial simulation of electric double layer overlap effects in devices combining micro- and nanochannels," *Microfluidics and Nanofluidics,* vol. 5, pp. 761-774, Dec 2008.

[70] Y. S. Choi and S. J. Kim, "Electrokinetic flow-induced currents in silica nanofluidic channels," *Journal of Colloid and Interface Science,* vol. 333, pp. 672-678, May 2009.

[71] Z. Siroma, *et al.*, "Depression of proton conductivity in recast Nafion (R) film measured on flat substrate," *Journal of Power Sources,* vol. 189, pp. 994-998, 2009.

[72] D. M. Bernardi and M. W. Verbrugge, "A MATHEMATICAL-MODEL OF THE SOLID-POLYMER-ELECTROLYTE FUEL-CELL," *Journal of the Electrochemical Society,* vol. 139, pp. 2477-2491, Sep 1992.

[73] S. J. Paddison, *et al.*, "High frequency dielectric studies of hydrated Nafion (R)," *Journal of Electroanalytical Chemistry,* vol. 459, pp. 91-97, 1998.

[74] J. G. Santiago, "Electroosmotic flows in microchannels with finite inertial and pressure forces," *Analytical Chemistry,* vol. 73, pp. 2353-2365, May 2001.

[75] A. Persat, *et al.*, "Basic principles of electrolyte chemistry for microfluidic electrokinetics. Part II: Coupling between ion mobility, electrolysis, and acid-base equilibria," *Lab on a Chip,* vol. 9, pp. 2454-2469, 2009.

[76] A. Persat, *et al.*, "Basic principles of electrolyte chemistry for microfluidic electrokinetics. Part I: Acid-base equilibria and pH buffers," *Lab on a Chip,* vol. 9, pp. 2437-2453, 2009.

[77] D. R. Lide, Ed., *CRC Handbook of Chemistry and Physics*. 2010, p.^pp. Pages.

[78] D. Sinton, *et al.*, "Effects of liquid conductivity differences on multi-component sample injection, pumping and stacking in microfluidic chips," *Lab on a Chip,* vol. 3, pp. 173-179, 2003.

[79] S. J. Kim, *et al.*, "Concentration polarization and nonlinear electrokinetic flow near a nanofluidic channel," *Physical Review Letters,* vol. 99, p. 4, Jul 2007.

[80] U. Bohme and U. Scheler, "Effective charge of bovine serum albumin determined by electrophoresis NMR," *Chemical Physics Letters,* vol. 435, pp. 342-345, 2007.

[81] H. Lin, *et al.*, "Instability of electrokinetic microchannel flows with conductivity gradients," *Physics of Fluids,* vol. 16, pp. 1922-1935, 2004.

[82] J. J. Santos and B. D. Storey, "Instability of electro-osmotic channel flow with streamwise conductivity gradients," *Physical Review E,* vol. 78, 2008.

[83] B. D. Storey, *et al.*, "Electrokinetic instabilities in thin microchannels," *Physics of Fluids,* vol. 17, 2005.

[84] S.-M. Ahn and R. J. Simpson, "Proteomic Strategies for Analyzing Body Fluids," in *Proteomics of Human Body Fluids: Principles, Methods, and Applications,* V. Thongboonkerd, Ed., ed: Humana Press Inc.

[85] N. L. Anderson and N. G. Anderson, "The human plasma proteome - History, character, and diagnostic prospects," *Molecular & Cellular Proteomics,* vol. 1, pp. 845-867, Nov 2002.

[86] G. L. Hortin and D. Sviridov, "The dynamic range problem in the analysis of the plasma proteome," *Journal of Proteomics,* vol. 73, pp. 629-636, Jan 2010.

[87] S. L. S. Freire and A. R. Wheeler, "Proteome-on-a-chip: Mirage, or on the horizon?," *Lab on a Chip,* vol. 6, pp. 1415-1423, 2006.

[88] H. Chen and Z. H. Fan, "Two-dimensional protein separation in microfluidic devices," *Electrophoresis,* vol. 30, pp. 758-765, Mar 2009.

[89] K. D. Huang and R. J. Yang, "A nanochannel-based concentrator utilizing the concentration polarization effect," *Electrophoresis,* vol. 29, pp. 4862-4870, Dec 2008.

[90] R. Dhopeshwarkar, *et al.*, "Transient effects on microchannel electrokinetic filtering with an ion-permselective membrane," *Analytical Chemistry,* vol. 80, pp. 1039-1048, Feb 2008.

[91] T. C. Kuo, *et al.*, "Manipulating molecular transport through nanoporous membranes by control of electrokinetic flow: Effect of surface charge density and debye length," *Langmuir,* vol. 17, pp. 6298-6303, Oct 2001.

[92] D. C. Duffy, *et al.*, "Rapid prototyping of microfluidic systems in poly(dimethylsiloxane)," *Analytical Chemistry,* vol. 70, pp. 4974-4984, 1998.

[93] J. C. McDonald, *et al.*, "Fabrication of microfluidic systems in poly(dimethylsiloxane)," *Electrophoresis,* vol. 21, pp. 27-40, 2000.

[94] J. Monahan, *et al.*, "A method for filling complex polymeric microfluidic devices and arrays," *Analytical Chemistry,* vol. 73, pp. 3193-3197, Jul 2001.

[95] M. Napoli, *et al.*, "Nanofluidic technology for biomolecule applications: a critical review," *Lab on a Chip,* vol. 10, pp. 957-985, 2010.

[96] B. Hoyer, *et al.*, "Effect of the pretreatment of recast Nafion membranes on their rejection of the albumin interference in anodic stripping voltammetry," *Electroanalysis,* vol. 13, pp. 843-848, 2001.

[97] G. B. Li, *et al.*, "A quantitative model to evaluate the ion-enrichment and ion-depletion effect at microchannel-nanochannel junctions," *Analytica Chimica Acta,* vol. 650, pp. 214-220, 2009.

Appendix A
MatLab Code for the Numerical Solution of the Poisson Boltzmann Equation

```
function pb6
```

Variables

```
c0 = 10;  %Bulk concentration [mol/m^3]
conc = logspace(-5,6);  %Concentration range used to calc. zeta_a range
sigma_s = -300e-3;  %surface charge density [C/m^3]

F = 96485.34;  %Faraday's Constant
T = 298;  %Temp. [K]
k = 1.381e-23;  %Boltzmann's constant
e_charge = 1.602e-19; %Charge of electron
e0 = 8.85e-12;  %Permittivity of vacuum
er = 45;  %relative permittivity of water
z1=1;  %valence of counter-ion
z2=-1; %valence of co-ion

d = 5e-9;  %Channel diameter
N = 1000;  %Number of data points (plot resolution)
y = linspace(0.0001,1,N);

lambda = 2/d*(e0*er*k*T/(e_charge*c0*F*(z1-z2)))^.5;  %non-
dimensionalized debye length
sigma = sigma_s*d*e_charge*(z1-z2)/(4*e0*er*k*T);  %non-dimensionalized
surface charge
```

Numerical Evaluation

```
%Numerically solve the Poisson-Boltzmann equation using BVP4C (Boundary
%Value Problem)
%------------------
%initial conditions correspond to flat potential
solinit = bvpinit(y, [asinh(sigma*lambda^2*z1/2),sigma]);
sol = bvp4c(@twoode, @twobc, solinit);

phi = deval(sol,y);  %assign solution for potential

phi0 = phi(1,end); %phi0 = zeta potential

phiy = 2*k*T/(e_charge*(z1-z2))*phi(1,:); %dimensional form of
potential phi
phiy(1,end)
2*trapz(y,y.*phi(1,:))*2*k*T/(e_charge*(z1-z2))
f = 2*trapz(y,y.*phi(1,:));
zeta = (phi0 - f)*2*k*T/(e_charge*(z1-z2)); %apparent zeta potential

%integrand for integral factor (Santiago's method)
fi2 = exp(-2*(z2/z1)/(1-z2/z1)*phi(1,:));

c2=c0*(-z1/z2)*exp(-(2*z2/z1)/(1-(z2/z1))*phi(1,:));
c1=c0*exp(-2/(1-(z2/z1))*phi(1,:));
```

Averaged Values

```
f2 = 2*trapz(y,y.*fi2(1,:));

cb2= c0*(-z1/z2)*f2

cb =-2/z1*sigma_s/(d*F) - z2/z1*cb2
```

Apparent Zeta

```
%Calculate apparent zeta over range of concentrations
 za = zeta_a(conc);
%
% %Create curve fit for zeta apparent points
 [estimates, model] = zeta_plot(conc,za);
 estimates
%
 figure(3)
 semilogx(conc, za,'*')
 hold on
 [sse, curve] = model(estimates);
 semilogx(conc, curve,'r')
```

Plots

Create figure

```
figure1 = figure;

% Create axes
axes1 = axes('Parent',figure1,'FontSize',12,'FontName','Calibri');
% Uncomment the following line to preserve the X-limits of the axes
 %ylim(axes1,[-25 25]);
hold(axes1,'all');

% Create multiple lines using matrix input to plot
set(plot(c2,y*d/2*1e9),'Color',[1 0 0],'DisplayName','co-ion');
set(plot(c1,y*d/2*1e9),'Color',[0 0 1],'DisplayName','counter-ion');

% Create title
title('Concentration Distribution','FontSize',16,'FontName','Calibri');

% Create xlabel
xlabel('Concentration (Mol/m^3)','FontSize',14,'FontName','Calibri');

% Create ylabel
ylabel('Channel Height (nm)','FontSize',14,'FontName','Calibri');

figure(2)
plot(d/2*y*1e9,phiy(1,:)*1000)
title('Potential Distribution')
xlabel('Channel Height (nm)')
ylabel('Potential (mV)')
```

Function declarations

```
%------------------------------
    function dUdy = twoode(y,U)
```

```
        %lambda = 2/d*(e0*er*k*T/(e_charge*c0*F*(z1-z2)))^.5;

        dUdy = [U(2)
            -1/(2*lambda^2)*(exp(-2/(1-z2/z1)*U(1)) - exp(-2*z2/z1/(1-
z2/z1)*U(1)))-U(2)/y];
    end
%------------------------------
    function  surf = twobc(dphia, dphib)

       %sigma = sigma_s*d*e_charge*(z1-z2)/(4*e0*er*k*T);

        surf = [dphia(2)
            dphib(2) - sigma];
    end
%------------------------------
    function  [estimates, model] = zeta_plot(xdat, ydat)
        start = [0,1,-1];
        lambda_d = (e0*er*k*T./(e_charge*conc*F*(z1-z2))).^.5;
        model = @z;
        estimates = fminsearch(model, start);
        function [sse, Curve] = z(a)
            Curve = a(1)*(1-tanh(-log(lambda_d)/a(2) +a(3)));
            Error = Curve - ydat;
            sse = sum(Error.^2);
        end
    end
%------------------------------
    function za = zeta_a(c)
        %Take a range of concentrations and calculate the apparent zeta
        %values and plot them
        %
        n = length(c);
        %iterate throught the concentrations solving the PB boundary
value
        %problem
        for i = 1:n
            lambda = 2/d*(e0*er*k*T./(e_charge*c(i)*F*(z1-z2))).^.5;

            solinit = bvpinit(y, [asinh(sigma*lambda^2*z1/2),0]);
            sol = bvp4c(@twoode, @twobc, solinit);
            phi = deval(sol,y);
            phi0 = phi(1,end);
            f = 2*trapz(y,y.*phi(1,:));
            za(i) = (phi0 - f)*2*k*T/(e_charge*(z1-z2));
        end
    end
end
```

Appendix B
Parameters and MatLab Code for Determining Effective Voltage

```
function v_appl
sigma_bulk = 488e-6; %S/cm
sigma_naf = 0.00145; %S/cm
sigma_depl = sigma_bulk/200; %S/cm

%top channel
L_channel = 5; %mm
A_channel = 0.4*0.04; %mm^2

%hole
L_hole = 2.5; %mm
D_hole = 0.200; %mm
A_hole = pi*D_hole^2/4; %mm^2

%Radial chamber
L_chamber = 1.2; %mm
A_chamber = 2*pi*0.6*0.02; %mm^2

%nano
L_nano = 0.2; %mm
h = 50e-6; %mm
A_nano = 2*pi*1.4*h; %mm^2

%OuterRadial
L_outer = 0.15; %mm
A_outer = 2*pi*1.575*0.02; %mm^2

%ground
L_ground = 0.94; %mm
A_ground = 0.1*0.02; %mm^2


R1 = res(sigma_bulk,L_channel, A_channel);
R2 = res(sigma_bulk,L_hole,A_hole);
R3 = res(sigma_bulk,L_chamber,A_chamber);
R4 = res(sigma_naf,L_nano,A_nano);
R5 = res(sigma_bulk,L_outer,A_outer);
R6 = res(sigma_bulk,L_ground,A_ground);

Rng = res(sigma_naf,L_ground,A_ground);
R6 = 1/(1/R6+1/Rng);

Rnc = res(sigma_naf,L_chamber,A_chamber);
R3 = 1/(1/R3+1/Rnc);

%depletion
Rd_full = res(sigma_depl,L_chamber,A_chamber);
Requivf = 1/(1/Rd_full + 1/Rnc);

V0i = (R3+R4+R5+R6)/(R1+R2+R3+R4+R5+R6)
V0d = (Requivf+R4+R5+R6)/(R1+R2+Requivf+R4+R5+R6)

V0g = (R6)/(R1+R2+R3+R4+R5+R6)
```

```
V0dg = (R6)/(R1+R2+Requivf+R4+R5+R6)

V_appli = 400*V0i - 400*V0g
V_applf = 400*V0d-400*V0dg
    function R = res(sigma,L,A)
        R = 1/sigma * L/A *10;
    end

end
V0i =

    0.4133


V0d =

    0.4144


V0g =

    0.1771


V0dg =

    0.1768


V_appli =

   94.4614


V_applf =

   95.0727
```